NOVAFCSH
FACULDADE DE CIÊNCIAS SOCIAIS E HUMANAS
UNIVERSIDADE NOVA DE LISBOA

UAV DATA MODELING FOR GEOINFORMATION UPDATE

Paulo José Arnaldo Albuquerque

Dissertação de Mestrado em Ordenamento do Território e Sistemas de Informação Geográfica

Setembro, 2022

Dissertação apresentada para cumprimento dos requisitos necessários à obtenção do grau de Mestre em Ordenamento do Território e Sistemas de Informação Geográfica, realizada sob a orientação científica do Professor Doutor José António Tenedório e do Professor Doutor Nelson Ribeiro Pires.

Aos meus pais,

pelo apoio.

À Beatriz,

pelo propósito.

ACKNOWLEDGEMENTS

UAV DATA MODELING FOR GEOINFORMATION UPDATE

Paulo José Arnaldo Albuquerque

[RESUMO]

A dissertação visa avaliar a relevância e o desempenho dos dados obtidos por Veículos Aéreos Não Tripulados (VANT) na atualização de Geoinformação. Os dados obtidos por VANT serão utilizados quer em conjunto com outros dados – obtidos por plataformas tradicionais de deteção remota –, quer isoladamente, recorrendo à técnica de *Structure from Motion* (SfM), para gerar o modelo digital de superfície e os ortomosaicos de alta precisão em diferentes momentos. Para a avaliação da precisão dos dados, os modelos digitais de terreno serão comparados. Por outro lado, os dados e informação gerados permitirão atualizar Geoinformação e quantificar as mudanças ocorridas no uso e ocupação do solo. Os resultados irão alimentar a discussão crítica da ação antrópica nos aglomerados urbanos e as propostas de intervenção.

[ABSTRACT]

The dissertation aims to assess the relevance and performance of data obtained by Unmanned Aerial Vehicles (UAVs) in updating Geoinformation. The data obtained by UAVs will be used either in conjunction with other data – obtained by traditional remote sensing platforms – or on its own, using the *Structure from Motion* (SfM) technique, to generate high-precision digital surface models and orthomosaics at different times. For the accuracy assessment of the data, the digital terrain models will be compared. On the other hand, the data and information generated will make it possible to update Geoinformation and quantify changes in land use and occupation. The results will feed the critical discussion of anthropic action in urban areas and intervention proposals.

PALAVRAS-CHAVE: Veículos Aéreos Não Tripulados (VANTs); Geoinformação; Atualizações.

KEYWORDS: Unmanned aerial vehicles (UAVs); Geoinformation; Updates.

TABLE OF CONTENTS

LIST OF ABBREVIATIONS

APA – Agência Portuguesa do Ambiente (Portuguese Environment Agency);

ASPRS – American Society for Photogrammetry and Remote Sensing;

CD – Change detection;

DEM[1] – Digital elevation model;

DSM – Digital surface model;

DTM – Digital terrain model;

GIS – Geographic information system;

GSD – Ground sampling distance;

LULC – Land use, land cover;

RMSE – Root mean square error;

RS – Remote sensing;

SfM – Structure from motion;

UAV – Unmanned aerial vehicle;

UHR – Ultra high resolution.

---

[1] Sometimes in the literature, the terms DEM, DSM and DTM are used interchangeably; however, within the scope of this work we will be using the definitions presented in https://geodetics.com/dem-dsm-dtm-digital-elevation-models/. DEM represents the bare-Earth surface, removed from all natural and built features; DSM represents both the natural and built/artificial features and DTM typically enhances a DEM, by including vector features of the natural terrain, such as rivers and ridges. A DTM may be interpolated to generate a DEM, but not vice versa.

1. INTRODUCTION

We live in the Information Age, where copious amounts of data (Big Data) are being collected every day to assist the decision making processes. Human settlements (particularly cities) are becoming very complex systems that require a lot of up-to-date information, which needs to be efficiently collected, analysed and properly managed. All this data has a geographical component attached. A famous quote in the GIS community states that *everything happens somewhere*.

"The increased reliance on geospatial data for decision-making in urban planning makes it imperative that the available spatial information is up-to-date and faithfully represents reality. This calls for map updating methods which support the integration of data from different sources in an automated manner". [1, p. 1]

"To ensure the usability of spatial data as well as to provide a solid basis for informed decision-making and planning, map updating is imperative". [2, p. 312]

Therefore, in Spatial Planning these concerns about data availability and quality are especially relevant. With our dissertation we intend to contribute to this debate and analyse the potentialities of UAV RS data modelling for the update of Geoinformation.

Traditional remote sensing platforms, like satellites and airplanes, have significant costs associated, require a great deal of planning and don't have a great temporal resolution. In the last decade, UAVs have increasingly been used as remote sensing platforms and offer much greater flexibility, not only for the possibility of using various sensors, but also for the ease of operation and the possibility of obtaining very high temporal resolutions.

Adão et al. (2017) referred to UAVs as a remote sensing platform capable of overcoming not only satellite but also manned aircraft issues by bringing enhanced spectral and spatial resolutions, operational flexibility and affordability to the users. [3]

UAVs are increasingly being used for a multitude of applications. For example: in agriculture, archaeology, environmental monitoring, mining, urban planning, 3D

modelling of historical buildings, emergency response, etc. Table 1 presents some UAVs' remote sensing applications.

Table 1. Overview of UAVs' remote sensing applications, adapted from [4, p. 11]

	Selected Applications	Highlights
Precision agriculture and vegetation	Soil property estimation; crop/vegetation management; forest structure assessment.	• Easily operated platforms; • High-spatiotemporal-resolution sensor data; Less impact of atmospheric factors; • Feasible access to high-resolution 3D structure of vegetation.
Urban environment and management	Traffic control; urban infrastructure management; building observation; urban environment mapping.	• Real-time monitoring of high dynamic objects; High visibility; • Higher redundancy & reliability; • Easily acquired 3D models of urban objects.
Disaster hazard and rescue	Post-disaster assessment; emergency responses; fire surveillance; landslide dynamic monitoring; coastal vulnerability assessment.	• Safer and lower-cost than in situ measurements; • Quick response; • Integrated sensor data bring more effective interpretation.

This thematic has been researched in the last years, and the literature suggests that there is a great potential for UAV data. For example, Haala et al. (2013), estimating the quality of 3D point clouds obtained from UAV data, remarked how "UAVs are becoming standard platforms for photogrammetric data capture especially while aiming at large scale aerial mapping for areas of limited extent". [5, p. 183]

The authors' research "demonstrated the feasibility of relatively simple UAV-platforms and cameras for 3D point determination in the sub-pixel level. Absolute elevation accuracies in the order of ½ GSD [Ground Sample Distance] of the captured imagery could be verified for very complex topographic areas". [5, p. 188]

Not only are UAVs a very practical (and easily deployable) data gathering platform, but they are also capable of achieving great accuracy, as long as some precautions are taken, namely the use of GCPs. Sanz-Ablanedo et al. (2018) observed how the "geometrical accuracy of georeferenced digital surface models (DTM) obtained from images captured by micro-UAVs and processed by using structure from motion (SfM) photogrammetry depends on several factors, including flight design, camera quality, camera calibration, SfM algorithms and georeferencing strategy. (…) the accuracy improves as the number of GCP points increases (…)". [6, p. 1]

More recently UAV RS data started to be fused with data from other RS platforms.

"Data fusion, as a general and popular multi-discipline approach, combines data from multiple sources to improve the potential values and interpretation performances of the source data, and to produce a high-quality visible representation of the data. Fusion techniques are useful for a variety of applications, ranging from object detection, recognition, identification and classification, to object tracking, change detection, decision making, etc. (…)

Remote sensing data fusion, as one of the most commonly used techniques, aims to integrate the information acquired with different spatial and spectral resolutions from sensors mounted on satellites, aircraft and ground platforms to produce fused data that contains more detailed information than each of the sources". [7, p. 5]

There are numerous fusion methods available. To name a few: fusion of multi-bands images, fusion of multispectral and panchromatic images, fusion of multispectral and hyperspectral images and the corresponding sub-methods to each of these methods (more details can be seen [8]). There are also different levels at which the fusion techniques can be applied: pixel level, feature level and decision level (more details can be seen in [7]).

Geoinformation updating is essentially a CD problem, but according to Tewkesbury et al. (2015), given the many methods in use, most authors seem to agree that there isn't a universal CD technique. The sheer number of change detection techniques and fusion methods makes it very difficult to consider any single one as the recommended technique/method. [9]

The objective of this dissertation is to assess the potential of UAVs' RS data and image fusion for Geoinformation updating, by applying some of the RS CD techniques and fusion methods to a case study. This dissertation is organized as follows: Section 1 gives an overview of what is to be accomplished; Section 2 reviews the state of the art; Section 3 presents the case study; Section 4 presents a comparison of the data; Section 5 presents a discussion of the results and lastly the final remarks are presented.

2. STATE OF THE ART

In recent years UAVs gained enormous relevance in remote sensing and pose a great alternative to the traditional methods. For example, Negash et al. (2019), analysing the use of UAVs in agriculture, observed how they "can offer high versatility and flexibility, as compared to satellites, and can operate rapidly without planned scheduling. Additionally, they can fly at low altitudes and slowly, with the ability to acquire spatial and temporal high-resolution data, representing important advantages against conventional platforms that have been broadly used over the years". [10, p. 254]

Kolarik et al. (2020), on their research on the assessment of vegetation structure using UAVs, also concluded that they offer an advantage over the traditional RS platforms, like satellites, since UAVs are not (as) constrained by atmospheric effects, cloud cover, temporal constraints, and seasonality. Since UAVs fly at low altitude they can acquire images with centimetre-level ground sampling distances (GSD), with much greater resolution than data collected via satellite platforms. [11]

There is a vast array of remote sensing techniques; however a major advantage of UAVs is that they allow for the use of Structure from Motion (SfM), a technique that is "able to produce 3D information from unstructured aerial images". [12, p. 6880]

SfM, also referred to as SfM-MVS (Multi-View Stereo) is a photogrammetry technique that "operates under the same basic tenets as stereoscopic photogrammetry, namely that 3-D structure can be resolved from a series of overlapping, offset images". [13, p. 301]

"SfM is the same method used to determine the relative position that a camera has with respect to another considered as fixed or reference, that is, it is the same method as computing the relative position between the two cameras". [14, p. 3]

Traditional photogrammetric methods require the exact location and pose of the cameras used and/or the coordinates of a series of control points. However, SfM doesn't require these data since "the geometry of the scene, camera positions and

orientation is solved automatically without the need to specify a priori, a network of targets which have known 3-D positions". [13, p. 301]

"While classic photogrammetric methods typically rely on strips of overlapping images acquired in parallel flight lines, SfM was designed to restitute the three-dimensional geometry of buildings and objects from randomly acquired images. As in the case of classic photogrammetry, the only caveat is that each physical point on the restituted object be present in multiple images". [15, p. 422]

Despite the similarities between SfM and conventional photogrammetry, SfM is not "simply an incremental development in photogrammetry" [16, p. 251]. SfM was developed in the 1990s, "has its origins in the computer vision community and the automatic feature-matching algorithms" were developed in the previous decade [13, p. 301]. Although some aspects of SfM derive "from advances in 3D computer vision algorithms, (…) photogrammetric principles and techniques are embedded in the SfM-MVS workflow". [16, p. 251]

"Instead of using the analog airphoto stereopairs with overlap along the flight path, the Structure from Motion process starts by acquiring photographs of the object of interest with sufficient overlap (e.g. 80–90%) from multiple positions and/or angles. Based on advances in image feature recognition, such as the Scale Invariant Feature Transform (Lowe, 2004), the common points are automatically detected and matched between photographs. A bundle block adjustment is then performed on the matched features to identify the 3D position and orientation of the cameras, and the XYZ location of each feature in the photographs resulting in a sparse 3D point cloud (Snavely, Seitz, & Szeliski, 2008; Triggs, Mc Lauchlan, Hartley, & Fitzgibbon, 2000)". [17, p. 281]

Mancini et al. (2013), comparing the SfM approach on coastal environments with Terrestrial Laser Scanning (TLS) and Global Navigation Satellite Systems (GNSS) confirmed "the high performance of the SfM methods applied to images acquired by the UAV system" [12, p. 6892]. They noted how SfM "applied to images acquired by a low-altitude UAV system produced a point cloud and derived DSM representing a

beach dune system with high topographic quality and vertical accuracy, comparable with GNSS survey data". [12, p. 6895]

The SfM technique has also proven to be very effective in situations where there is greater spatial complexity. For example, Sadeepa Jayathunga et al. (2020), in their study of the potential of UAV photogrammetry for characterization of the forest canopy structure, concluded that SfM not only facilitated the 3D modelling of the forest canopy, but was also more cost-effective than Light Detection and Ranging (LiDAR) data. The authors also found strong correlations between "field and UAV-SfM structural metrics (…) [that indicate] that the UAV point cloud data have the potential to capture the variations of the actual forest canopy structure, such as size and size variation". [18, pp. 66, 67]

Sanz-Ablanedo et al. noted how a "strong photogrammetric network" needs "highly redundant imagery" and "diversity in camera roll angles", specifically the introduction of oblique images. [6, p. 6]

Some researchers have already directly compared SfM with other traditional – high accuracy – methods. Grohmann et al. (2020) set out to compare the accuracy of airborne LiDAR (Light Detection and Ranging), ALS, terrestrial LiDAR, TLS, and SfM-MVS (MultiView-Stereo) in the detection of dune migration and volume change. The authors concluded that SfM-MVS is a good alternative to the other methods. "Besides a good correlation to the TLS DEM, the full SfM-MVS DEM shows a good fit with elements of the landscape that did not experience significant change between the surveys, such as the road bordering the dune field to west and southwest". [19, p. 7]

In Portugal, Gómez-Gutiérrez & Gonçalves (2020) used two UAVs (multirotor and fixed wing) to survey coastal cliffs in Praia do Porto da Calada. They concluded that the "multirotor platform and SfM-MVS photogrammetry was found to provide the best cliff coverage (…)". [20, p. 8171]

Callow et al. (2018), in their study of coastal sediment archives, noted how the "availability, low-cost and utility of remotely piloted aircraft systems (…), allows overlapping image collection over geomorphic features for SfM applications (herein termed 'RPAS-SfM' [Remotely Piloted Aircraft System - SfM]). RPAS-collected multiple

overlapping digital images allow the combined use of Structure-from-Motion (SfM) photogrammetric techniques to produce datasets at higher resolution and lower cost than airborne LiDAR, and at comparable resolution and accuracy but at lower costs and more efficiently relative to TLS, particularly for complex terrain (Niethammer et al., 2012; Turner et al., 2012; Mancini et al., 2013; Colomina and Molina, 2014)". [21, p. 2604]

The authors also made a reference to the fact that LiDAR surveys are "limited to what the sensor can 'see' for each scan, which requires multiple scans and more ground control, generating large datasets and significant processing challenges". [21, p. 2604]

In their study, they concluded that UAVs and SfM "provide new insight into earth surface processes and geomorphic features". [21, p. 2613]

Despite the evident strides in the development of SfM (and LiDAR), there are concomitant technologies/techniques being explored, namely Convolution Neural Networks (CNNs). CNNs are an example of Artificial Intelligence being applied – with high accuracy, regardless of the intrinsic uncertainty of the processes – to the analysis and classification of images. CNNs "work on different self-defined filters which allow creation of point based network simulating neuron connections in human brain, making then the final decision about attribution of image to certain category or class". [22, p. 3]

Gebrehiwot et al. (2019) described how they trained CNNs to, automatically and with great accuracy, label UAV images used for flood mapping. For this, the authors used Fully Convolutional Networks (FCNs).

Dang et al. (2020) also used CNNs (with an accuracy of about 98%) in their attempt of coastal classification in Vietnam. They "proposed the use of a convolutional neural network (ConvNet) for coastal classification based on these technologies and geomorphic profile graphs. The primary input data is digital elevation/depth models obtained from ALOS and NOAA satellite". [23, p. 11824]

"UAVs technology is an efficient photogrammetry data acquisition platform that can be used to quickly deliver high-resolution imagery for flood

assessment and emergency response. (…) In this study, the FCN-16s model was fine-tuned and trained to extract the inundated areas. (…) Experimental results indicated that a CNN-based classifier such as FCN-16s was very suitable in flood imagery segmentation with an overall accuracy of 95% and a Kappa index of 0.904". [24, p. 11]

RS data acquired with UAVs presents a set of characteristics – UHR, greater availability of spectral and geometric information, and integrated sensor data – that, compared to traditional RS data, allows for differentiated applications, greater accuracies and increased availability of datasets. Some of the existing methods/techniques used for traditional RS data are reusable and fine-tuned to address UAV RS data; however, there is a need for more tailored analysis techniques. [4]

For example, LULC mapping, one of the main applications for UAV RS data, faces some challenges when dealing with UAV imagery. The UHR allowed by UAV-borne sensors has a centimetre-level GSD that turns small objects – normally imperceptible to traditional RS platforms – into objects of interest "(such as pedestrians on the street, cars, infected plants, weed patches, and dustbins)". [4, p. 8]

A method to improve LULC classification accuracy is to fuse UAV RS data with data from other RS platforms (some examples are presented in table 2). For achieving better accuracy, geometric and spectral information should be combined. UAV photogrammetric data can very easily generate DSMs, using the SfM technique, and these can be fused with other datasets. However, since the scale difference between objects (the same or different ones) can be significant, there is a need to employ multi-scale approaches (at the feature or image level). As the scene complexity increases some classifiers are no longer capable of performing efficiently (e.g.: SVM, Random Forest, and Maximum Likelihood) and there is a need for more advanced classifiers. These can be a combination of simpler classifiers, or deep learning-based methods: fully convolutional networks; convolutional neural networks (e.g.: U-Net); Pyramid Scene Parsing Network (PSPNet), etc. [4]

In remote sensing the purpose of data fusion is to integrate information acquired from different sensors (from multi-platforms) at different spectral and spatial

resolutions, and produce a result where the fused data contains more information than each of the sources. [7]

	LULC Mapping	Change Detection
Low-to-moderate-resolution satellite RS data	• Pixel-based classification; • Data transformation such as principal component analysis or empirical object indices; • Occasionally applied object-based analysis for very large objects; • Objects can be approximated by single pixels; • Mixed pixel effects.	• Pixel-based analysis approaches; • Radiometric normalization or reflectance computations are essential; • Object-based analysis is occasionally used for large objects; • Post-classification methods.
High-to-very high-resolution satellite or airborne data	• High inter-pixel similarity and high intra-pixel variance; • Pixel-based methods are still used; • Object-based methods with textural features; • Semantic/contextual information can be implemented; • Deep learning-based methods are used for scene analysis.	• Co-registration of images is essential and algorithms handling misalignment can be a key for images with suboptimal camera networks for dense matching; • Object-based methods are primarily used, as it is slightly more robust to misalignment; • Shape/textural features are important for difference analysis; • 3D change detection can be applied for stereo data, while stereo data might not often be available.
Ultra-high-resolution UAV-borne data	• Very high inter-pixel similarity and high intra-pixel variance; • Object-based analysis is essential and Super-pixel based methods are often used; • The need for fusing 3D information such as height, geometric and oblique information for remote sensing analysis; • Contextual information and deep learning methods are essential for accuracy improvement.	• Data co-registration is less problematic as most of the UAV data are photogrammetrically acquired and comes with associated 3D information by applying rigorous multi-view matching methods; • The need for analyzing the 3D uncertainty for geometric comparison; • The need for fusing 3D and spectral information for change determination; • Contextual information and deep learning methods are essential for accuracy improvement.

Multi-source data fusion techniques have increasingly been applied in diverse fields, from remote sensing to computer vision, medical image processing, security and defence, and others. However, in remote sensing, the techniques still present challenges when applied to multi-source data with variable spatial and temporal resolutions. Data fusion techniques in remote sensing can essentially be classified into three different levels: pixel/data level, feature level and decision level. [7]

A schematic representation of the three different levels of data fusion can be seen in figures 1 through 3.
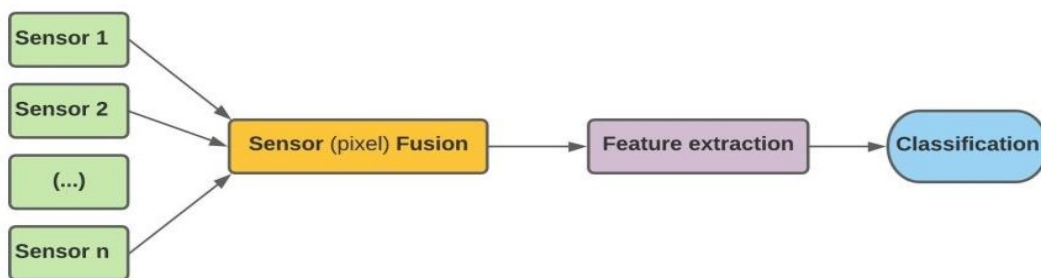

Figure 1 – Pixel level fusion, adapted from [25, p. 77]
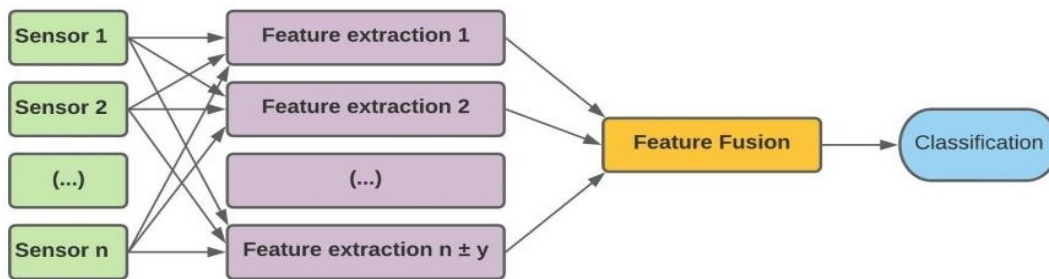
Figure 2 – Feature level fusion, adapted from [25, p. 77]
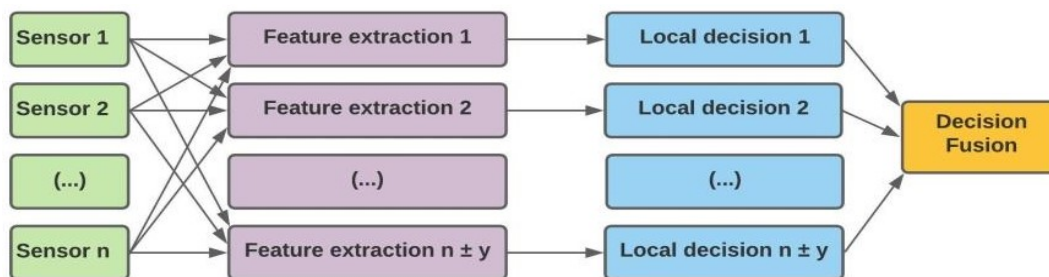
Figure 3 – Decision level fusion, adapted from [25, p. 77]

The fusion process must fulfil three criteria: "preservation of all relevant information, elimination of irrelevant information and noise, and minimization of artefacts and inconsistencies in the fused image". [25, p. 78]

At the pixel level, two or more geometrically co-registered images (of the same scene) are combined into a single image that presents more information than the originals. The images may originate from the same or different sensors and have the same or different spatial and spectral resolutions. Multispectral images have higher spectral resolution and lower spatial resolution than panchromatic images. The fusion process generates images with the highest spectral and spatial resolutions. [25]

Feature level fusion occurs at a higher level than pixel fusion. The process consists of the extraction of features from the RS images and a subsequent fusion of those features. The objects are extracted using segmentation. "Features correspond to characteristics, which are depending on their environment such as shape, extent and neighborhood, are extracted from the original images. The similar objects from multiple sources are assigned to each other and then fused for further assessment". [25, p. 82]

Decision fusion occurs at the highest processing level. In this process the input "images are processed individually for information extraction. Then, the decision rules are used to combine extracted information to reinforce common interpretation and resolve differences and furnish a better understanding of the observed objects. The input decisions are some labels or symbols with different degrees of confidence". [25, p. 84]

Zhang (2010) defines pixel level fusion as "the combination of raw data from multiple sources into single resolution data, which are expected to be more informative and synthetic than either of the input data or reveal the changes between data sets acquired at different times; feature level fusion as capable of extracting various features, e.g. edges, corners, lines, texture parameters, etc., from different data sources and then combines them into one or more feature maps that may be used instead of the original data for further processing; and decision level fusion as a combination of the results from multiple algorithms to yield a final fused decision and if the results from different algorithms are expressed as confidences (or scores) rather than decisions, it is called soft fusion; otherwise, it is called hard fusion. Methods of decision fusion include voting methods, statistical methods and fuzzy logic-based methods". [7, p. 6]

Joshi et al. (2016), in their review of radar and optical remote sensing data fusion (for land use mapping and monitoring) observed a vast methodological difference in the analysed studies and didn't find "a particular rationale explaining the stage at which fusion between radar and optical datasets was performed [pixel, feature or decision level] (…) or in the inputs and types of classification techniques utilized, for the target aims of the reviewed studies". [26, p. 15]

They concluded their review with some remarks urging the development of: "(ii) robust techniques to fuse optical and radar data across different ranges of temporal and spatial resolutions, tested over the same study regions and within the same land use themes to ease the comparability of results; (iii) systematic and standardized procedures for assessing the accuracy and benefits of fusing data sources; and (iv) studies conducted over larger spatial scales, supported by efficient

computational processing capacity and permanent ground-based sites for calibration and validation". [26, pp. 17, 18]

In the context of using UAVs' RS data for the update of Geoinformation the main focus seems to rest with the fusion of optical datasets. However, data fusion in remote sensing remains a relatively new research field, and new fusion techniques are still being developed and tested.

For example, Dian et al. (2019) proposed a novel – pixel level – technique for fusing a high spatial resolution multispectral image (HR-MSI) with a low spatial resolution hyperspectral image (LR-HSI). The authors proposed a spatial-spectral sparse representation (SSR) approach with the goal of obtaining a high spatial resolution hyperspectral image (HR-HSI) from the fusion of an HR-MSI and an LR-HSI (the algorithmic approach is explained in [27]). Nirmala & Vaidehi (2015) also proposed new pixel and feature level image fusion methods. They employed a Non Sub-sampled Contourlet Transform (NSCT) "for multi-resolution decomposition as it is demonstrated to capture the intrinsic geometric structures in images effectively" [28, p. 743]. They proposed two pixel-level fusion methods (one using NSCT with fuzzy logic and another using NSCT and SVM) and a feature-level fusion method using NSCT and AdaboostSVM (a detailed explanation of these methods can be found in [28]).

Tian & Wang (2009) analysed the different levels of image fusion and proposed ten evaluation parameters to assess the fused images: entropy, mutual information, average gradient, standard deviation, cross entropy, unite entropy, deviation and relative deviation, mean square error, root mean square error – RMSE, and *Peak-To-Peak Signal-To-Noise Ratio* – PSNR. The algorithms for each parameters as well as the specific use of each indicator can be seen in [29]. According to the authors, pixel-level fusion is "the most important and the most fundamental multi-sensor image fusion method" since it produces images with much richer information at the most basic (pixel) level, that allows for better analysis and processing results, even if the images are used as inputs in other fusion levels/methods. [29, p. 246]

Ghassemian (2016) presented three approaches for the assessment of fused products: a first approach that doesn't need a reference image and uses "quality indexes"; a second approach that "considers the images at a spatial resolution lower

than the original and considers the original MS image as a reference (Wald's protocol)"; a third approach that doesn't need a reference image and the "approximations of MS and PAN images are obtained *from the fused images"*, then each of the approximated images (MS and PAN) is compared with the respective original image. [25, p. 85]

Li et al. (2017) reviewed the state of the art of pixel-level image fusion and analysed some of the major pixel-level image fusion methods, the adopted transforms and respective fusion strategies (a detailed analysis can be seen in [30]). They identified four major methods: multi-scale decomposition; sparse representation; methods in other domains (e.g.: IHS, PCA, Gram-Schmidt transform, ICA, gradient domain, and fuzzy theory); and combination of different transforms. They also presented two major classes of evaluation metrics for fused images: a) objective evaluation metrics requiring a reference image and b) objective evaluation metrics without requiring a reference image.

For a), some of the proposed metrics are: the RMSE; the PSNR; the *erreur relative globale adimensionnelle de synthèse* (ERGAS) index. Despite the used evaluation metrics, the authors found that "there are still many unresolved problems". First, the evaluation metrics don't respond the same way to every fusion method; second, there isn't a good solution to evaluate the image quality of cross-resolution images; third, most of the existing evaluation metrics cannot be directly applied to multi-channel images (colour, multispectral, hyperspectral) or three-dimensional data. [30, p. 105]

For b), the authors categorized the evaluation metrics into two major groups: "(1) information theory based metrics, which only consider how much information is transferred from inputs to the fused image, and (2) local feature based fusion metrics, which evaluate the relative amount of features (sensitive to human vision system) that is transferred from the input images to the fused image" [30, p. 106]. In this class there are also some problems to be solved. First, most of the existing metrics only work with grey images and may perform poorly with colour images (with multiple channels) because they do not account for colour distortions; second, in some applications, the images may contain noise or image blurring and the existing metrics are not

generalized enough to deal with these situations; third, the real-time implementation of quality assessment methods remains a challenging problem. [30]

Even with the difficulties that still affect pixel-level fusion, the authors concluded that it is "one of the most important techniques to integrate and analyze information from multiple sources". [30, p. 110]

From this brief analysis of the state of the art it can be concluded that UAVs are a proven alternative to traditional remote sensing platforms. Not only are the technological advantages very compelling, but there are also some subjective advantages. For example, Andriolo et al. (2020), referring to coastal dunes monitoring, consider that UAVs are "an optimal solution for a non-intrusive survey on the fragile dune environment". [31]

However, Geoinformation update requires not only the data acquisition step, but also the appropriate analysis procedures. These are the procedures used for CD, since "change detection is one of the most important subjects in remote sensing" ([32], [4]).

A particularly important concept in CD is the temporal trajectory, which represents a multi-year series of radiometrically calibrated anniversary spectral data. This temporal trajectory translates the spectral behaviour of corresponding land cover elements over time. [33]

Deus & Tenedório (2021) analysed the LULC change trajectories for the Portimão municipality (Algarve, Portugal) over a 71 years period (1947-2018), concluding that knowing the past and current spatial dimension, pattern, and location of LULC change trajectories is crucial to understand territorial sustainability and anticipate possible futures. [34, p. 19]

The authors also drew attention to the need for further research regarding multi-temporal and multi-resolution components, as well as the use of 3D data.

"Future research on this approach that combines LULC change trajectory analysis and spatial pattern metrics needs to focus on analysing to what extent the quantitative and analytical results of LULC change detection are affected using multitemporal and multi-resolution imagery as data sources.

It should also focus on enriching this approach with the creation of new spatial pattern metrics based on 3D data". [34, p. 19]

UAVs are a proven RS platform with an increasing number of sensor being deployed, a myriad of techniques being developed and seem the perfect RS tool for the evaluation of temporal trajectories. Nevertheless, despite all the advantages, it is crucial to guarantee the quality of the data.

2.1. QUALITY OF THE INFORMATION

Quality of the information is a universal requirement, but this gains a particular significance in photogrammetry. Given its spatial nature, the scales and uncertainties associated with the data, great care needs to be implemented to avoid a situation of *garbage in, garbage out*.

Before exploring some of the problems that may affect the quality of the information, a few remarks about scale and uncertainty are in order.

In cartography, scale refers to the mathematical relation between the size of an object in the real world and its size on a map. However, in spatial data analysis, this concept can be contradictory: "a map which covers the whole of the Earth is termed small scale, but an investigation which covers the whole planet is termed large scale". [35, pp. 10, 11]

> "An image with small pixels has high resolution, while one with big pixels has low resolution. In this regard, scale is synonymous with the level of detail of an image (…). Scale is also commonly used to refer to the scope or extent of a study area. A large scale of study area (such as a country), if mapped, implies a small-scale map, whereas a small scale of study area (such as a city), if mapped, implies a large scale map. Obviously, confusion and frustration arise from multiple, seemingly contradictory meanings, and how to translate statistical inferences across scales". [36, p. 1]

Lloyd (2013) also made a distinction between the various concepts of scale in spatial data analysis: 'operational scale' – "scale over which a process operates" – and a scale that relates to 'spatial extent'. This 'spatial extent' scale is further divided into

two elements: 'scales of spatial measurement' and 'scales of spatial variation', where the 'scale of spatial measurement' consists of two parts: "(i) the support (geometrical size, shape and orientation of the measurement units) and (ii) the spatial coverage of the sample". [35, pp. 10, 11]

The support/spatial coverage distinction is extremely important, especially in remote sensing settings, since it can determine the accuracy (level of uncertainty) of the data being collected. Using the example presented by Lloyd (2013), we can observe – figures 4 and 5 – how two maps of the same area (same spatial coverage) present very different spatial variation, given the different size of the cells used (different support).
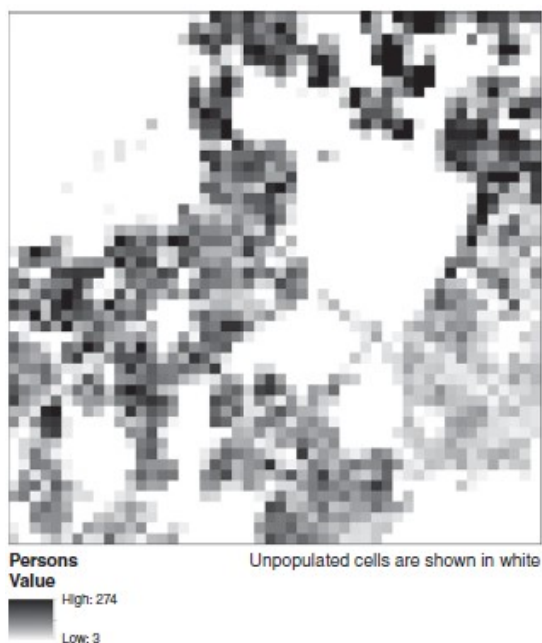
Figure 4 – Persons by 100m grid cell; adopted from: [35, p. 12].
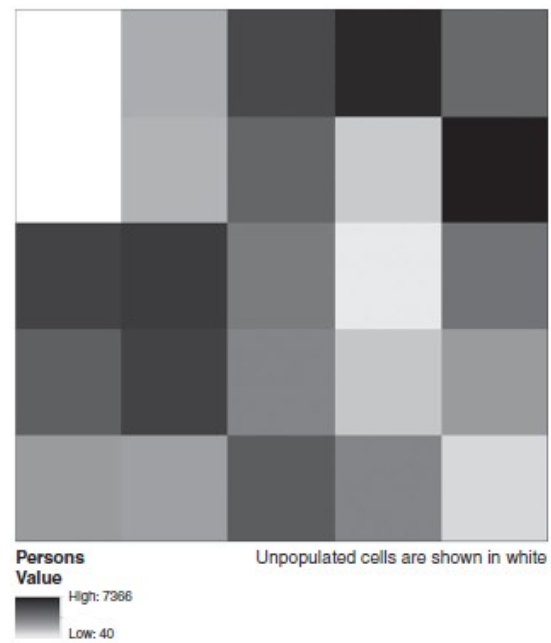
Figure 5 – Persons by 1km grid cell; adopted from: [35, p. 12].

This simple example illustrates how scale and uncertainty are closely related and shows that before any data is even collected, uncertainty is already being introduced into the process.

Other important concepts are spatial autocorrelation and spatial dependence. Tobler's first law of geography states: *everything is related to everything else, but near things are more related than distant things*. The spatial autocorrelation "tends to vary over different spatial scales, and characterising the relationship between distance and difference is a core approach in the analysis of spatial scale". [35, p. 13]

Lloyd (2013) used the example of a DEM to explain the connection between spatial autocorrelation and scale. A DEM representing a mountainous region may have a great variation of elevation values for points very close together, while a DEM of a river floodplain may present a small elevation variation even between points separated by large distances.

"Most environmental processes are scale dependent (Atkinson and Tate 2000), and therefore, the observed spatial variation is likely to differ as the spatial scale of measurement varies. This means that there is a need to identify a sampling strategy that enables identification of spatial variation of interest". [35, p. 13]

"Physical processes, or the outcomes of those processes, are a function of multiple complex interacting factors which operate at different spatial scales. Spatial variation of soil and geological properties occurs at a wide range of spatial scales (…)". [35, p. 23]

Another question is that scale should not be uniquely analysed from a Euclidean space perspective. In reality, most geographical features have a fractal nature. A famous quote by Benoit Mandelbrot states: *Clouds are not spheres, mountains are not cones, coastlines are not circles, and bark is not smooth, nor does lightning travel in a straight line*.

This fractal nature of things has large implications on the concept of scale. Jiang et al. (2016) stressed how the "major concern surrounding scale is how it affects geospatial data collection and analysis results with respect to accuracy and reliability. (…) Unfortunately, most geographic features are not measurable, or the measurement is scale-dependent because of their fractal nature (…), the length of a coastline, the area of a lake, and the slope for a topographic surface are all scale-dependent, so they should not be considered absolute". [36, p. 2]

According to the authors, fractal geometry "aims for a scale-free or scaling that involves all scales (…) [, where] scale-free is synonymous with scaling, literally meaning no characteristic mean for all sizes. (…) It is fair to say that both Euclidean and fractal geometries aim to characterize things, but with different means; the former through

measurement (at one scale), and the latter through scaling (across all scales)". [36, p. 4]

Although the previous paragraphs already suggest a relation between scale and uncertainty, uncertainty is not simply a function of scale. It could be argued that it is a universal characteristic.

In reality, uncertainty is present in any system, no matter how simple. If we were to look at one of the building blocks of the universe, the atom, we would find uncertainty ingrained in it. The classical atomic model (where the electrons orbited the nucleus as if they were planets) has long been replaced by a theoretical model where the electrons can be found – without absolute certainty – in a probabilistic cloud surrounding the nucleus. This holds true not only for very small scales, but also for a very large ones, e.g., the trajectories of planets in our solar system are chaotic in nature when more than two bodies are present.

In geography, uncertainty has been researched in the last decades and some authors, like Couclelis (2003) and Fusco et al. (2017), used GIS as a framework to address it.

Couclelis (2003) approached uncertainty based on the notion of "that which cannot be known". Using mathematical concepts like Russell's paradox, Gödel's incompleteness theorem and borrowing from physics' Heisenberg's uncertainty principle, the author revealed the universal nature of uncertainty and its obvious intrusion into 'Geospatial Knowledge'.

"Indeed, the mathematics of chaos and complexity theory have helped clarify what can and cannot be known in the case of complex nonlinear systems. (…)Wolfram (2002) and others have shown that deterministic chaos is a common behavior in systems modeled as cellular automata, a formalism now widely used by environmental scientists". [37, p. 168]

Even Artificial Intelligence is affected by this uncertainty pervasiveness. Couclelis (2003) noted how the "field of knowledge representation in artificial intelligence has come up with its own 'impossibility theorems' that stem directly from these formal limits to knowledge, while applying very generally to the everyday

knowledge construction that geospatial researchers and practitioners engage in". [37, p. 169]

The author concluded that error in geographic information "is inevitable, and not just because of human limitations". She proposes a "systematic 'encyclopedia of ignorance' for geospatial knowledge", in order "to map out the ultimate terra incognita of epistemic impossibility". [37, p. 173]

Building upon Couclelis' (2003) paper, Fusco et al. (2017) identified "eight domains within the activity of the geographer, where questions of uncertainty arise: geographic information, geographic definitions, the explanation of geographic phenomena, the complexity of spatial systems, geosimulation, the representation of spatial knowledge, subjectivity in spatial phenomena, and planning". [38, p. 2261]

For our research problem we are particularly interested in the uncertainty that affects geographic information. Fusco et al. (2017) stated that uncertainty "appears in the incoherences between the modelling primitives of GIS and real spatial information, in data granularity, in spatio-temporal aggregation and disaggregation of data (…). Sometimes data are already affected by error functions, when they are derived from measurement or sampling procedures". [38, p. 2262]

The authors concluded that "the practical and theoretical impossibility of predicting the future state of a geographic system brings researchers to more general conceptions of uncertainty, which go well beyond questions of data validity and error management. Traditional probabilistic modelling of uncertain events is also reconsidered, as the fitting of probabilistic laws seems less and less justified (…)".[38, p. 2274]

In Fusco et al.'s (2017) opinion, "geographers should accept uncertainty as a necessary component of the research activity and results". Priority should be given to probable "uncertainties in explanations, concept and model definitions", and the creation of "models of complex systems should not aim at replicating the simple sensitivity to parameter approach of classical models". [38, pp. 2274, 2275]

Other authors, like Comber et al. (2007) chose remote sensing as a framework, since they find remote sensing to be an "inherently uncertain exercise due to the spectral and spatial limitations of remotely sensed imagery". [39, p. 5]

Comber et al. (2007) pointed the Boolean classification of datasets as a major factor for uncertainty as parameters like spatial and spectral resolutions may introduce uncertainty in the identification of classes. According to the authors "there is a growing interest in being able to reallocate data objects into different classes for different landscape questions: context sensitive maps. The re-allocation may be based on the uncertainty associated with the original Boolean allocation and/or due to different weights being given to the supporting evidence, for instance from ancillary data". [39, p. 2]

The authors discussed how uncertainty in GIS is approached with probabilistic models that don't take into consideration the interdependency between different pieces of data and evidence. This approach is problematic for three reasons: "First, the much environmental data is spatial auto-correlated. Second, the classic error assessment method, tabulating predicted against observed in a correspondence matrix, assumes that like is being compared with like. This is not the case. (…) Third, the landscape objects themselves are assumed to [be] well defined (i.e. not vague, indeterminate or ambiguous – see Fisher et al, 2006) and can therefore be assessed using, crisp probabilistic measures to give measures of error". [39, p. 2]

The problem with the identification of classes is illustrated in figures 4, 5 and 6. Figure 6 gives some more insight into the type of errors introduced in function of the scales adopted.

These errors, or fallacies – according to Jiang et al. (2016) –, occur because although geographic features (natural and manmade) are fractal in nature, this only holds for a limited scaling range. For example, using figure 6, panel a) for illustration purposes, we can see that if we kept using smaller and smaller yardsticks we would end up with an infinite perimeter, but a finite area. At some point – scale dependent – it is not practical to keep adding complexity to the contour, but this is translated into an error/inaccuracy in the measurement – and this measurement needs to be performed as if the element is Euclidean –. "The length of a linear geographic feature

such as a coastline is not measurable. To be more precise, the measurement depends on map scale or image resolution". [36, p. 5]
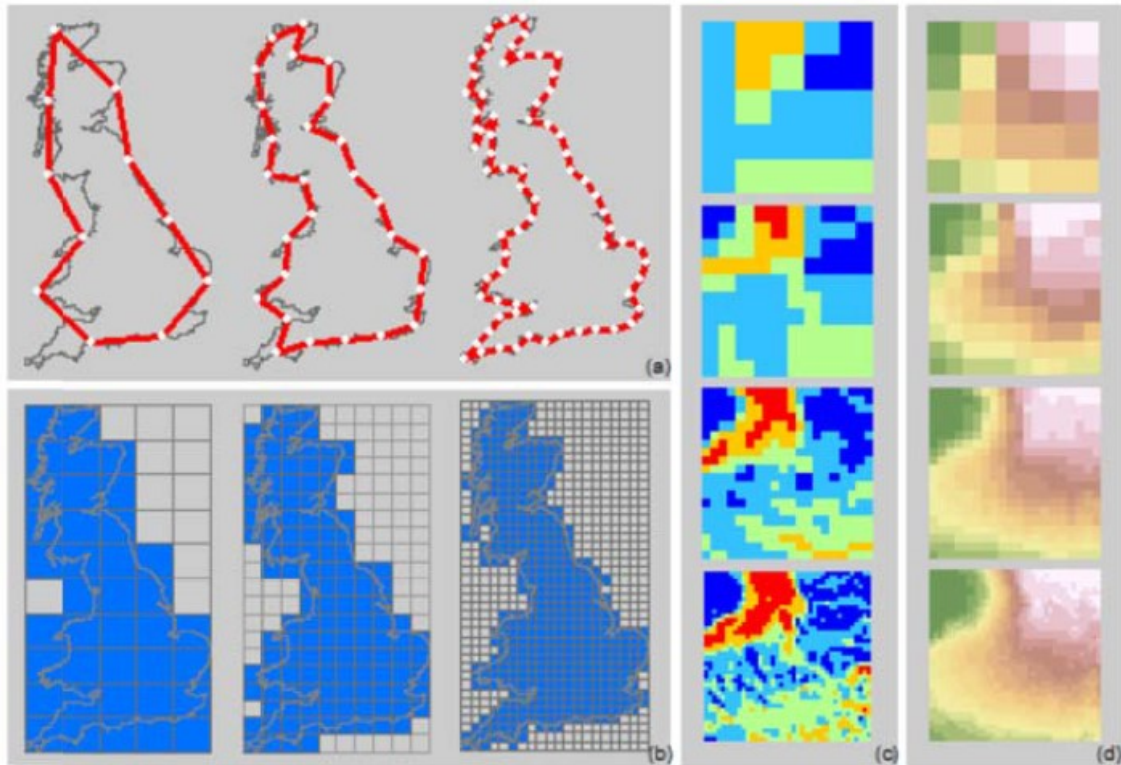
Figure 6 – Illustration of how measurement changes with scales. In panel a) we observe how the length of the coastline changes with different yardstick scales. In panel b) we observe how the area of the island changes with scale. In panel c) we see how the slope (and the number of classes) changes with scale. On panel d) we can observe how DEM resolutions are affected by scale. Adopted from [36, p. 5]

After this preamble on uncertainty and scale, some of the issues that affect the quality of UAVs' RS data will be analysed. For example, weather conditions can compromise the accuracy of UAVs' RS data in several ways. Strong winds can alter flight trajectories and cause sharp variations in altitude, pitch, roll and heading. This situation alone can compromise a significant part of, if not all, the collected data. Alves Júnior et al. (2018) reported some of these issues, namely a 45 degree rotation of the photographs in relation to the flight line.

"This angular variation is known as 'crab' and is caused by the wind blowing at the side of the plane. To keep to the route as defined, the aircraft rotates the prow toward the opposite direction of the wind. Therefore, the

aircraft will move parallel to the flight line, with its prow pointing to a direction that is different from what was initially designed for the flight line". [40, p. 8]

Another condition that may be influenced by weather, but is intrinsic to all electronic equipment, is temperature.

Daakir et al. (2019) researched the effects of temperature variation in digital cameras. "When a camera is subject to a variation of temperature, it undergoes a deformation which impacts the internal parameters. It is recommended to use metric cameras with stable camera internal parameters. The quality of internal geometry modeling impacts directly the photogrammetric accuracy". [41, p. 142]

"Investigations carried out with an aerial camera show that the effect of temperature change induces a variation of focal length of 0.5 μm per degree [0.068 pixels] for a Nikor lens of 20mm [2575 pixels] (Merchant, 2006, 2012). Merchant adds: 'For a flight with a height of 2000m above ground, this (focal length variation) corresponds to a systematic elevation error of 1m compared to a position determined by GPS'". [41, p. 143]

Most drone mounted cameras are not metric. SfM algorithms can automatically estimate camera parameters, but this is an estimate. So, even before getting in the air and take any photos the system is already prone to uncertainty.

But the issues go beyond cameras' internal parameters and temperature.

"Any 3D surface model normally obtained by SfM photogrammetry is initially captured in an arbitrary reference system. Geo-referencing involves transforming this initial arbitrary datum into a predefined coordinate reference system. This can be done either directly using known exterior orientations of photographs ("direct geo-referencing") or by providing appropriate coordinates to points (ground control points or GCP) that are recognizable in the photographs ("indirect geo-referencing"). Direct geo-referencing requires the measurement of the coordinates of the camera at the exact moment the picture is acquired, which is a challenge because the unmanned vehicle is moving, often with a velocity of several meters per second. With this movement, it is difficult to perfectly synchronize the camera triggering with the

sampling frequency of the Global Navigation Satellite System (GNSS) receiver. If the integer ambiguities of the satellite and receiver ranges are not resolved, it is also obviously difficult to freeze the motion of the UAV in-flight whilst a GNSS solution is established. Finally, it is impossible to collect several epochs at each point to improve the position accuracy. Despite its convenience, this method of geo-referencing can therefore achieve only decimeter to meter accuracies, even for very high-resolution projects". [6, p. 2]

Sanz-Ablanedo et al. (2018) drew attention to the necessity of using GCPs to reduce the "dome" deformation that SfM may produce. "It has become recognized that processing vertical imagery with automated SfM procedures can generate an error surface in the form of a systematic dome feature (…).These deformations can be reduced by using GCP (…)". [6, p. 2]

However, GCPs alone don't solve all problems. When GCPs are used, the SfM generated model conforms to the GCPs coordinates, but this doesn't imply that every point on the 3D model has accurate coordinates: "evaluating the accuracy of a georeferenced model using control points is not fully objective, since the shape of the model adapts to the control points, and consequently GCP will always achieve the lowest residuals. Using check points provides a far more objective quantification of the true accuracy of geo-referencing procedures". [6, p. 3]

Just as important as the use of, is the placement of the GCPs. "In UAV-SfM photogrammetry where non metric cameras are used, the best option is to try to distribute the GCP evenly or homogeneously in the periphery but also in the center of the area (…)". [6, p. 7]

Sanz-Ablanedo et al. (2018) concluded that the "geometric accuracy of an SfM photogrammetric 3D model is highly dependent on the ground georeferencing strategy, and the results of this study confirm that the accuracy is strongly dependent on the number of GCPs introduced in the bundle adjustment (BA)". [6, p. 14]

The authors also found that, for their research, the "optimum accuracies are achieved when GCPs are evenly distributed around the whole area. To concentrate GCPs in specific areas, to leave gaps without GCPs or to concentrate points on the

periphery or in the center seem to be strategies that will not derive good accuracies. Ideally, GCPs should be distributed in a triangular node grid, since this distribution will minimize the maximum distance of any point to the nearest GCP". [6, p. 14]

They also presented a strategy to implement when check points are not available. It estimates the real accuracy by multiplying the RMSE obtained from the GCPs by a given factor, dependent on the number of GCPs. [6, p. 17]

Scale, for all the reasons already presented, is also a very important factor in data accuracy, especially for data fusion. Usually the images to be fused present very different spatial scales and this factor alone can, and will, introduce uncertainty to the entire process.

Li et al. (2017) noted how "there still exist many challenges in image fusion and objective fusion performance evaluation, resulting from image noise, resolution difference between images, imperfect environmental conditions, computational complexity, moving targets, and limitations of the imaging hardware". [30, p. 110]

Another problem is the spectral discrepancy in high resolution images. "For the fusion of optical images, a high image resolution corresponds with a large spectral discrepancy between neighbour pixels". [7, p. 17]

These issues will be further analysed in section 5. The next section looks at the Geoinformation update process.

2.2. UPDATING GEOINFORMATION

The need for updating Geoinformation arises from the occurrence of spatial changes; therefore CD is a vital concept in this process.

RS CD is an ever growing research field that is disparate and presents a high variability [9]. The various techniques employed are mainly based in two approaches: pixel-based or object-based. Each of these approaches is further divided into sub-methods; however, some authors found that these are similar, if not identical [9]. The main issue seems to lie with the unit of analysis (that should be based on the application scale and the resolution of the available images) [9]. A major disadvantage

of the pixel-based change detection methods is the inability to provide a spatial context for the real-world objects [42], however they remained the norm because of the lack of computing power and the scarcity of data. Nowadays these are no longer issues, and hybrid approaches and multi-temporal image-objects seem to be the most robust analysis units [9].

Machine Learning is currently a very valuable tool used in the analysis and processing of the large data sets and Data Mining techniques also presents a great potential to tackle the challenges of traditional techniques applied to very high resolution images. [42]

Wang et al. (2020) noted the high efficiency of bi-temporal image analysis, but also addressed some of the problems with this practice. They pointed out how CD, carried out at the pixel level, "may corrupt or even dominate the true change signal depending on its strength (…). [But since] images are not directly compared to each other during the land change detection process, radiometric and phenology differences could be well resolved". [43, p. 2]

According to the authors, the primary challenge occured from the binary nature of the CD process. "For binary land change detection, image pixels are divided into two categories, Change (C) and No Change (NC), adopting various statistical techniques such as thresholding or hypothesis testing". [43, p. 2]

They referred the difficulty of choosing threshold values and the arbitrariness of some of those values. They also pointed out that change is a dynamic process and the data collected should be three-dimensional. "Not only the spatial heterogeneity, but also the temporal characteristic of land change scenarios should be considered for spatial sampling". [43, p. 2]

Wang et al. (2020) also emphasized the uncertainty in CD: "Errors and uncertainties are build-in imperfections in ICD [Image Change Detection] and make it hard to make accurate decision in a chaotic situation (…)". [43, p. 8]

The authors pointed out some of the difficulties they experienced with bi-temporal analysis. The "assumptions of identical image situations are critical", but many assumptions don't seem to have been carefully checked. They noted how, at the

pre-processing stage, despite the adoption of photometric calibrations, the Landsat solar geometry was not available per pixel and the TOA (top of atmosphere) adjustments didn't vary per pixel. It was also assumed that the majority of classes remained unchanged between the paired images "so that the spectral statistical features of land classes remain unchanged between two dates, which is also hard to guarantee". Land change is a dynamic process and the use of RS images to characterize this process introduces uncertainty since land dynamics "are more appropriately viewed as fuzzy phenomena". Binary CD interprets land dynamics "either as abrupt change (the complete replacement of one cover type by another, also called 'real change') or as subtle change (the modification of land cover without changing its overall classification, also called 'pseudo change')". However, subtle changes have "spectral variance caused by the phenology problem (cyclical changes in the condition of the ground cover that do not relate to class change)". [43, p. 9]

"Detection of image differences may be confused with problems in phenology and cropping, and such problems may be exacerbated by limited image availability, poor quality in temperate zones (…). (…) To minimize phenology effect, it is practical to adopt two pairs of images, one pair within leaf-on season and the other within leaf-off season to mask the area of subtle change [5]". [43, p. 9]

As previously stated CD is a "disparate" process that "presents a high variability". Therefore, updating Geoinformation is also a disparate process with high variability. It is necessary to take into account the issues described to minimize the uncertainty of the data.

In the next sections the case study will be presented and the data compared.

3. CASE STUDY

For our case study we chose the Aguçadoura beach, in the municipality of Póvoa do Varzim, in the north of Portugal. The area is identified in figures 7 to 9.

This region was selected because APA is currently monitoring some sections of the Portuguese coastline and Aguçadoura is one of the regions being surveyed. This allowed access to official datasets that meet the accuracy standards required by ASPRS.
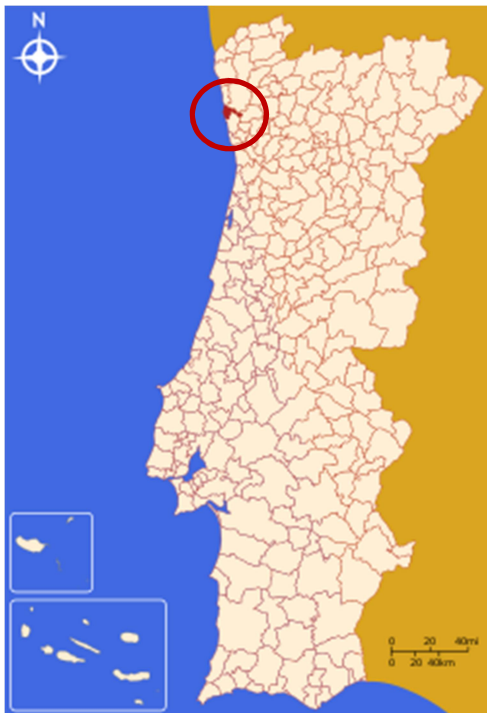
Figure 7 – Aguçadoura region*

Figure 8 – Aguçadoura*

Figure 9 – Area of interest (own orthophotomap), with GCPs and clipping polygon overlaid.

* – both images from: https://portugalfotografiaaerea.blogspot.com/2019/05/praia-de-agucadoura-praia-da-barranha-e.html

3.1. METHODOLOGY

The goals are threefold. First, qualitatively assess an UAV survey of the area of interest without the use of GCPs, to get an estimation of the associated errors. Second,

compare the generated orthophotomaps with APA's orthophotomaps. Third, fuse UAV data with satellite remote sensing data and compare it with the original satellite data.

Figure 10 shows a schematic of our methodology.
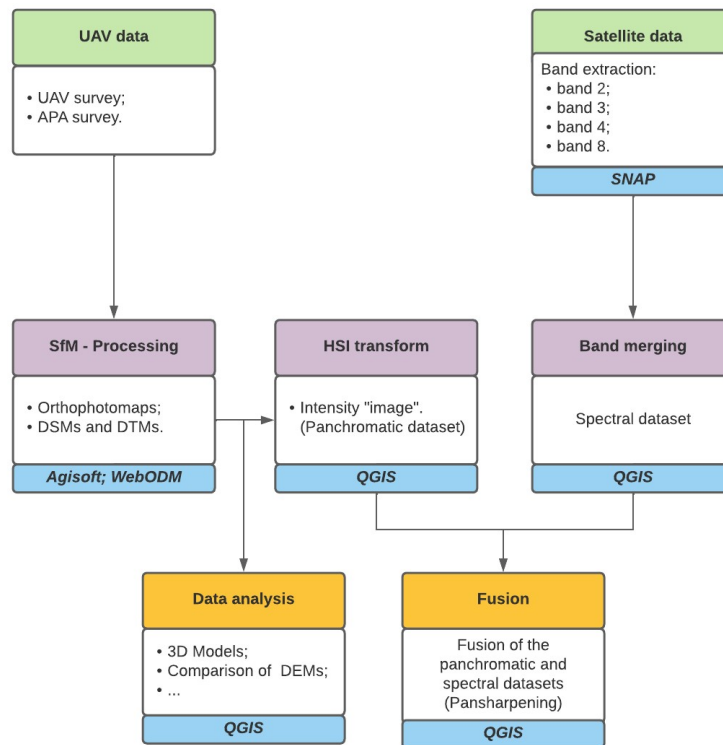
Figure 10 – Methodology schematic

We were granted access to some of APA's datasets[2] for the area of interest, specifically:

- ▪ The photos for both UAV surveys carried out by APA (28/02/2021 and 11/02/2022);

- ▪ The orthophotomaps and DSMs for both periods, processed by APA using the Pix4D software;

- ▪ A list of GCPs that included 5 points in our area of interest.

To assure that all datasets intersected the polygon presented in figure 9 was used to clip all the rasters.

---

[2] More details in annex

The UAV RS data from APA's surveys and ours were processed with Agisoft Metashape and WebODM. From this operation the orthophotomaps and DSMs – presented in the next sections – were created, which allowed for the operations described in section 4.

For two of the orthophotomaps an HSI (Hue, Saturation and Intensity) transform was applied to obtain the Intensity dataset. This is the recommended procedure when a panchromatic image is required for the fusion step.

Spectral bands from Sentinel 2 datasets were extracted using the SNAP software and later merged in QGIS.

The fusion of both datasets (Sentinel 2 merged bands and Intensity dataset) was performed with a pansharpening operation in QGIS. This procedure fused both datasets, at the pixel level, and the result was an image with the spatial resolution of the Intensity dataset and the spectral resolution of the merged dataset (band 2, 3, 4 and 8). The fused datasets were used to evaluate the NDVI index and compare the results with the RS satellite data.

3.2. UAV DATA

The UAV data presented in this work were collected in three different periods. The details can be seen in table 3. The DSMs presented in table 3 are just for illustration purposes. The areas are not homogeneous since APA's surveys were conducted along a relatively narrow strip of coastline. Our survey area was wider and shorter (hence the need to use the clipping polygon shown in figure 9).
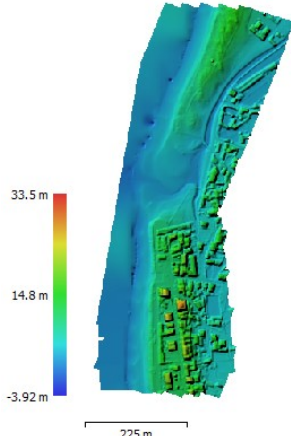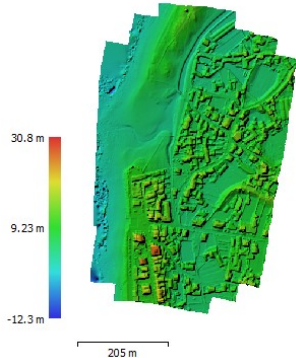
The resulting orthophotomaps can be seen in figures 11 through 19. Although APA provided the orthophotomaps processed in Pix4D, it was decided to also process the images with WebODM and Agisoft Metashape software to have a better term of comparison. However, for accuracy assessment a base map was required. Since access to vector data for the area of interest was not possible, the 2021 APA orthophotomap was used as the base map.

For our survey data, only WebODM and Agisoft Metashape software were used for image processing.

Two orthophotomaps were created with WebODM, one without GCPs and another with four GCPs. Although five GCPs are inside our area of interest, one of them (number 5, in figure 9) wasn't used because it was not possible to identify it in the photos (it was placed under a parked vehicle).

Two orthophotomaps were also created with Agisoft Metashape, one based on the generated DSM, the other on the DTM.

Table 3. UAVs datasets details

Dataset	Date and flight details	Photographs used	DSM (Agisoft)	Processing software

APA	28/02/2021
	
	Drone: DJI Matrice 300 RTK
	
	Camera: FC6310R (8.8mm))
	
	Flight altitude: 89,8 m
	
	GSD:
	  ▪ 2,40 cm (Pix4D);
	  ▪ 2,22 cm (Agisoft);
	  ▪ 2,20 cm (WebODM).
		353		• Pix4D
				• Agisoft Metashap
				• WebODM

APA	11/02/2022
	
	Drone: DJI Matrice 300 RTK
	
	Camera: ZenmuseP1 (35mm)
	
	Flight altitude: 131 m
	
	GSD:
	  ▪ 1,51 cm (Pix4D);
	  ▪ 1,51 cm (Agisoft);
	  ▪ 1,50 cm (WebODM).
		391		• Pix4D
				• Agisoft Metashap
				• WebODM

Own	26/03/2022
	
	Drone: DJI Mavic Air 2
	
	Camera: FC3170 (4.5mm)
	
	Flight altitude: 134 m
	
	GSD:
	  ▪ 4,16 cm (Agisoft);
	  ▪ 4,20 cm (WebODM).
		88		• Agisoft Metashap
				• WebODM

Figures 11 to 13 show the three orthophotomaps obtained from the same APA dataset, collected in 2021.

The three products have different pixel sizes because in WebODM and Agisoft Metashape the camera calibration parameters were performed automatically.

Figure 11 – APA 2021 (Pix4D), pixel size: 0,025x0,025m

Figure 12 – APA 2021 (Agisoft), pixel size: 0,022x0,022m

Figure 13 – APA 2021 (WebODM), pixel size: 0,020x0,020m

The same explanation is valid for the three orthophotomaps shown in figures 14 through 16.

The orthophotomaps in figures 17 to 19 were generated from our survey and the camera calibration parameters were also performed automatically by the software.

Figures 20 and 21 show two orthophotomaps generated with WebODM, the only difference being the inclusion of four GCPs (figure 21). For the same set of photographs, WebODM processed two different areas.

Figure 14 – APA 2022 (Pix4D), pixel size: 0,015x0,015m

Figure 15 – APA 2022 (Agisoft), pixel size: 0,015x0,015m

Figure 16 – APA 2022 (WebODM), pixel size: 0,020x0,020m

Figure 17 – Own survey (DSM – Agisoft), pixel size: 0,042x0,042m

Figure 18 – Own survey (DTM – Agisoft), pixel size: 0,042x0,042m

Figure 19 – Own survey (WebODM), pixel size: 0,038x0,038m

Although a quick observation might suggest few differences between the (same) datasets processed with different software, it will be shown in section 4 that there are somewhat significant differences.

Figure 20 – Orthophotomap generated with WebODM, no GCPs.

Figure 21 – Orthophotomap generated with WebODM, 4 GCPs.

These differences are the result of some of the issues previously addressed in section 2.

In addition to UAV data, satellite data were also used to characterize the area of interest. The objective was to fuse data from UAV and satellite RS and analyse the potential of the resulting products.

3.3. FUSION

The rationale behind fusing the Sentinel 2 and Intensity datasets, at the pixel level, is to obtain a resulting dataset that combines the information from the two original datasets and is more complete than either source.

Bands 2 (blue), 3 (green), 4 (red) and 8 (near infrared) were extracted from Sentinel 2 datasets and later merged in QGIS. This workflow is necessary to ensure that the final product has all the bands from the original dataset. Exporting all bands directly from SNAP, avoiding merging them individually later, results in a fused image without all the spectral information. The results are shown in figures 22 through 27.

Figure 22 – Merged bands (band 2, 3, 4 and 8) with RGB mask, pixel size: 10x10m, 28/02/2021.

Figure 23 – Intensity "image", obtained from APA's orthophotomap HSI transform, pixel size: 0,025x0,025m

Figure 24 – Fused dataset, with RGB mask, pixel size: 0,025x0,025m

The Sentinel 2 dataset for the 2021 period coincides with APA's survey date.

The Sentinel 2 images have a pixel size of 10 x 10 m. The intensity dataset has a pixel size of 0,025 x 0,025 m and a single band. The fused image has a pixel size of 2,5 cm and the four bands from the Sentinel 2 dataset.

For our UAV survey, it was not possible to obtain a suitable Sentinel 2 dataset for the same date, so a close one was chosen. The Sentinel 2 images were collected on 06/02/2022 and the UAV survey took place on 26/03/2022.

The intensity dataset has a pixel size of 0,041 x 0,041 m and a single band. The fused image has a pixel size of 4,1 cm and the four bands from the Sentinel 2 dataset.

Figure 25 – Merged bands (band 2, 3, 4 and 8) with RGB mask, pixel size: 10x10m, 06/022022

Figure 26 – Intensity "image", obtained from Agisoft's orthophotomap HSI transform, pixel size: 0,041x0,041m

Figure 27 – Fused dataset (Satellite and Agisoft datasets) with RGB mask, pixel size: 0,041x0,041m

A more in-depth analysis of these and other datasets will be carried out in section 4.

4. DATA COMPARISON

APA's datasets and ours will be further examined to show how the same dataset, depending on the processing algorithms, the number of GCPs, pre and post-processing steps, etc., can produce different results.

Figures 28 to 33 show the results of this analysis. The zoomed area is outlined in figure 28.

Figure 28 – APA 2021 (Pix4D), pixel size: 0,025x0,025m

Figure 29 – APA 2021 (Pix4D), pixel size: 0,025x0,025m

Comparing figure 29 with figures 31 and 33, it's possible to identify some of the differences.

In figure 29 three shadows of the same person can be seen. This is a result of the images being used by the processing algorithm in Pix4D. In figures 31 and 33 there is only one shadow present, but its location is different in both images. Again, this is the result of the images chosen by the processing algorithm in Agisoft Metashape and WebODM.

Figure 29 also shows evidence of some pre or post-processing step(s). Two vehicles present in figure 31 and 33 were removed in figure 29.

Figure 30 – APA 2021 (Agisoft), pixel size: 0,022x0,022m

Figure 31 – APA 2021 (Agisoft), pixel size: 0,022x0,022m

These first occurrences are not significant for the accuracy of the orthophotomap and were pointed out just to demonstrate how different software will use different images, from the same dataset, to create the same scene.

However, in figure 33 it's possible to observe some warpage in the façade of one building (pointed at red). This is a more problematic situation that may affect the accuracy of the orthophotomap.

As will be seen in the rest of this section, when datasets are compared and raster difference operations performed, this type of processing error may result in significant discrepancies in values.

This is due to some of the problems already listed in chapter 2. For some buildings, where part of the façade is visible, this means that either the processing algorithm was unable to create a true orthoimage, and/or the dataset didn't have any

oblique images. This type of error is common and may require post-processing stage(s).

Figure 32 – APA 2021 (WebODM), pixel size: 0,020x0,020m

Figure 33 – APA 2021 (WebODM), pixel size: 0,020x0,020m

As mentioned in section 2, regarding the use of GCPs, accuracy results for the GCPs can be somewhat misleading as the created orthophotomaps are adjusted to the given GCPs. "However, when RMSEs are calculated for the check points with the same combinations, a greater variation between the vertical and horizontal axes can be detected clearly". [6, p. 11]

As specified in section 3 the 2021 APA survey was used as a base map. Twelve check points were chosen from that dataset and later compared with the obtained locations on the other orthophotomaps. The RMSE was then calculated for those check points. Figures 34 and 35 illustrate the process for one of the check points.

Figure 34 shows the 2021 APA orthophotomap with 5 GCPs (yellow) and 12 check points (green). Figure 35 shows an instance with the location of the check points in all the orthophotomaps (details in table 4).

The 2022 APA orthophotomap (Pix4D) was accurate. Agisoft Metashape and WebODM, using GCPs, produced precise results. However, as expected for all the reasons previously stated, WebODM without GCPs produced a result that is not very accurate, especially in the Z coordinate.

Table 4. Check point details

Orthophotomap	X coordinate (m)	Y coordinate (m)	Z coordinate (m)
APA 2021 – Base map	**-54380,2926**	**195883,0576**	**9,555048943**
APA 2022 (Pix4D)	-54380,28527	195883,0494	9,553792953
Own (Agisoft)	-54380,21087	195883,0589	9,277898788
Own (WebODM)	-54380,20719	195882,9975	10,09000015
Own (WebODM) without GCPs	-54380,15414	195883,4832	15,97000027

Figure 34 – Base map with 5 GCPs (yellow) and 12 Check Points (green)
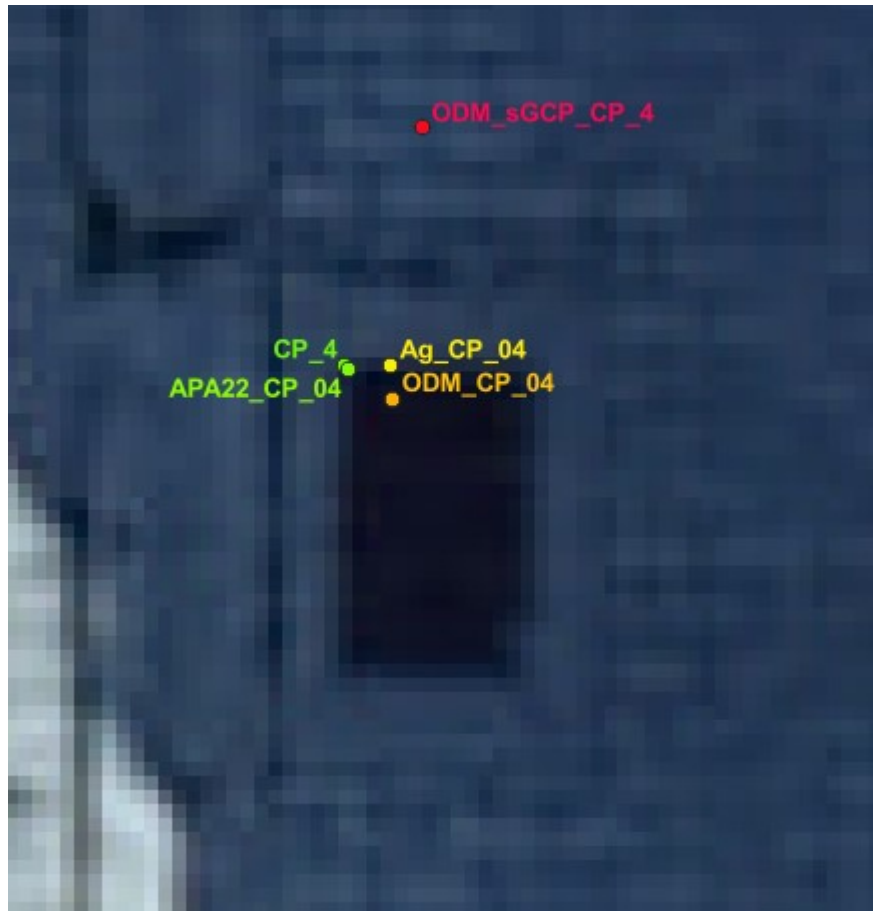

Figure 35 – Detail of Check Point 4 in all the orthophotomaps.

The processing reports generated by Agisoft Metashape and WebODM state the RMSE for the GCPs. These values are considerably lower than the values obtained for the check points.

Figures 36 and 37 show part of the reports generated by the Agisoft Metashape (left) and WebODM (right) software.
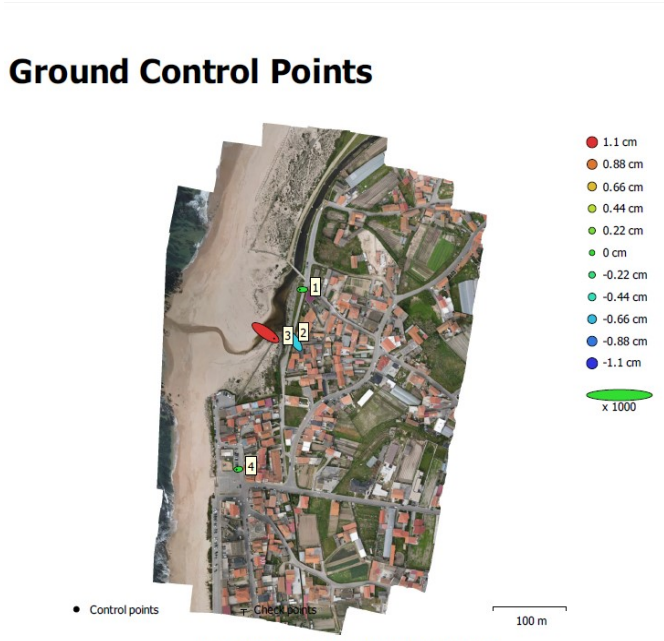

Ground Control Points

Fig. 4. GCP locations and error estimates.
Z error is represented by ellipse color. X,Y errors are represented by ellipse shape.
Estimated GCP locations are marked with a dot or crossing.

Count	X error (cm)	Y error (cm)	Z error (cm)	XY error (cm)	Total (cm)
4	1.35869	1.11923	0.62448	1.76032	1.86781

Table 4. Control points RMSE.
X - Easting, Y - Northing, Z - Altitude.

Survey Data

GPS/GCP/3D Errors Details

GPS	Mean	Sigma	RMS Error
X Error (meters)	-1.979	0.634	2.078
Y Error (meters)	-0.867	0.870	1.228
Z Error (meters)	-5.789	1.205	5.913
Total			6.286

GCP	Mean	Sigma	RMS Error
X Error (meters)	-0.000	0.001	0.001
Y Error (meters)	-0.001	0.001	0.001
Z Error (meters)	0.003	0.006	0.006
Total			0.004

3D	Mean	Sigma	RMS Error
X Error (meters)	0.013	0.015	0.020
Y Error (meters)	0.012	0.014	0.018
Z Error (meters)	0.026	0.039	0.047
Total			0.035

Figure 36 – Detail of Agisoft Metashape processing report

Figure 37 – Detail of WebODM processing report

Comparing the values in figures 36 and 37 with the calculated RMSE for the check points (tables 5 to 8) a significant difference is observed.

Table 5. Calculated RMSE for our own survey, processed with Agisoft Metashape. The real values were obtained from the 2021 APA survey.

	RMSE Agisoft									
Check Point	**X coordinates**				**Y coordinates**				**Z coordinates**			
	Real	Obtained	Residual X	Residual X²	Real	Obtained	Residual Y	Residual Y²	Real	Obtained	Residual Z	Residual Z²
1	-54348,4242	No data	No data	No data	195928,7281	No data	No data	No data	10,0594	No data	No data	No data
2	-54364,1133	-54364,1094	-0,0038	0,00001467	195922,2108	195922,2037	0,0072	0,00005144	10,0218	9,8877	0,1341	0,01798254
3	-54348,9393	-54348,9254	-0,0138	0,00019155	195908,4483	195908,4596	-0,0113	0,00012777	10,1960	10,0443	0,1517	0,02300566
4	-54380,2926	-54380,2109	-0,0817	0,00667963	195883,0576	195883,0589	-0,0013	0,00000166	9,5550	9,2779	0,2772	0,07681221
5	-54301,9266	-54301,9654	0,0388	0,00150322	195876,4610	195876,5462	-0,0851	0,00724676	8,6893	8,2221	0,4672	0,21828501
6	-54289,2387	-54289,3202	0,0815	0,00664662	195931,6649	195931,7335	-0,0687	0,00471410	6,8395	6,6185	0,2209	0,04881538
7	-54378,5469	-54378,3785	-0,1684	0,02836173	196017,1264	196017,0142	0,1121	0,01257632	9,5954	9,7361	-0,1408	0,01981430
8	-54294,5253	-54294,5451	0,0198	0,00039056	196022,6532	196022,6377	0,0155	0,00023983	5,5605	5,4403	0,1201	0,01442722
9	-54241,6293	-54241,6402	0,0109	0,00011976	196193,5093	196193,5437	-0,0344	0,00118395	5,6927	5,5518	0,1410	0,01987153
10	-54211,6193	-54211,6916	0,0724	0,00523994	196308,5090	196308,5104	-0,0014	0,00000197	5,1962	4,7000	0,4963	0,24627605
11	-54239,3079	-54239,3074	-0,0004	0,00000019	196306,3845	196306,3052	0,0793	0,00628492	5,1750	4,8336	0,3414	0,11653550
12	-54357,2679	-54357,1957	-0,0722	0,00521251	196046,5520	196046,4624	0,0896	0,00803187	9,6147	9,7431	-0,1283	0,01646596
			RMSE_X = 0,07029830				**RMSE_Y = 0,06064845**				**RMSE_Z = 0,27274553**	

RMSE_XY =	0,09284441
RMSE_XYZ =	0,28811492

Table 5 shows a RMSE_XY of approximately 9 cm, while Agisoft's processing report shows a value of approximately 1,9 cm.

A similar situation occurred for WebODM. The report states an RMSE_X of 1 cm, the same for RMSE_Y and an RMSE_Z of 4 cm. The total RMSE_XYZ is 4 cm. Comparing these values with those calculated for the check points, in table 6, a significant difference is observed, particularly for the Z coordinate, which is greater by a magnitude of ten.

Table 6. Calculated RMSE for our own survey, processed with WebODM. The real values were obtained from the 2021 APA survey.

Check Point	X coordinates				Y coordinates				Z coordinates			
	Real	Obtained	Residual X	Residual X²	Real	Obtained	Residual Y	Residual Y²	Real	Obtained	Residual Z	Residual Z²
1	-54348,4242	No data	No data	No data	195928,7281	No data	No data	No data	10,0594	No data	No data	No data
2	-54364,1133	-54364,1107	-0,0026	0,00000678	195922,2108	195922,1473	0,0636	0,00404380	10,0218	10,2000	-0,1782	0,03174564
3	-54348,9393	-54348,9205	-0,0187	0,00035141	195908,4483	195908,4265	0,0218	0,00047575	10,1960	10,5800	-0,3840	0,14747491
4	-54380,2926	-54380,2072	-0,0854	0,00729461	195883,0576	195882,9975	0,0600	0,00360452	9,5550	10,0900	-0,5350	0,28617280
5	-54301,9266	-54301,8513	-0,0753	0,00566900	195876,4610	195876,3990	0,0621	0,00385039	8,6893	9,8100	-1,1207	1,25590410
6	-54289,2387	-54289,2147	-0,0240	0,00057369	195931,6649	195931,6035	0,0613	0,00376373	6,8395	7,8400	-1,0005	1,00109226
7	-54378,5469	No data	No data	No data	196017,1264	No data	No data	No data	9,5954	No data	No data	No data
8	-54294,5253	-54294,4985	-0,0268	0,00072061	196022,6532	196022,5984	0,0547	0,00299584	5,5605	6,0100	-0,4495	0,20209491
9	-54241,6293	-54241,6218	-0,0075	0,00005556	196193,5093	196193,5866	-0,0773	0,00598084	5,6927	6,0300	-0,3373	0,11375573
10	-54211,6193	-54211,6119	-0,0073	0,00005380	196308,5090	196308,5533	-0,0443	0,00196515	5,1962	5,7500	-0,5538	0,30664439
11	-54239,3079	-54239,2081	-0,0998	0,00995649	196306,3845	196306,3064	0,0781	0,00609196	5,1750	5,4400	-0,2650	0,07023706
12	-54357,2679	-54357,2337	-0,0342	0,00116802	196046,5520	196046,5323	0,0197	0,00038850	9,6147	9,0200	0,5947	0,35372351
			RMSE_X =	0,05084286			RMSE_Y =	0,05758513			RMSE_Z =	0,61390922

RMSE_XY = 0,07681825
RMSE_XYZ = 0,61869667

The calculated values for the remaining orthophotomaps can be seen in tables 7 and 8.

Table 7. Calculated RMSE for 2022 APA's survey, processed with Pix4D. The real values were obtained from the 2021 APA survey.

Check Point	X coordinates				Y coordinates				Z coordinates			
	Real	Obtained	Residual X	Residual X²	Real	Obtained	Residual Y	Residual Y²	Real	Obtained	Residual Z	Residual Z²
1	-54348,4242	-54348,4242	0,0000	0,00000000	195928,7281	195928,7283	-0,0002	0,00000003	10,0594	10,0561	0,0033	0,00001095
2	-54364,1133	-54364,1377	0,0244	0,00059736	195922,2108	195922,2058	0,0050	0,00002528	10,0218	10,0076	0,0142	0,00020181
3	-54348,9393	-54348,9307	-0,0086	0,00007341	195908,4483	195908,4322	0,0160	0,00025659	10,1960	10,1810	0,0150	0,00022418
4	-54380,2926	-54380,2853	-0,0073	0,00005368	195883,0576	195883,0494	0,0082	0,00006677	9,5550	9,5538	0,0013	0,00000158
5	-54301,9266	-54301,9157	-0,0109	0,00011867	195876,4610	195876,4611	0,0000	0,00000000	8,6893	8,6653	0,0241	0,00057880
6	-54289,2387	-54289,2268	-0,0119	0,00014128	195931,6649	195931,6551	0,0098	0,00009539	6,8395	6,8059	0,0335	0,00112428
7	-54378,5469	-54378,4989	-0,0480	0,00230112	196017,1264	196017,1098	0,0166	0,00027524	9,5954	9,5848	0,0106	0,00011228
8	-54294,5253	-54294,5202	-0,0052	0,00002664	196022,6532	196022,6314	0,0218	0,00047443	5,5605	5,5612	-0,0007	0,00000055
9	-54241,6293	-54241,6210	-0,0082	0,00006784	196193,5093	196193,5055	0,0037	0,00001403	5,6927	5,6750	0,0177	0,00031380
10	-54211,6193	-54211,5981	-0,0212	0,00044978	196308,5090	196308,4900	0,0190	0,00036266	5,1962	5,1899	0,0063	0,00004015
11	-54239,3079	-54239,2723	-0,0356	0,00126720	196306,3845	196306,3365	0,0480	0,00230476	5,1750	5,1571	0,0179	0,00032137
12	-54357,2679	-54357,2523	-0,0156	0,00024376	196046,5520	196046,5283	0,0237	0,00055997	9,6147	9,6025	0,0122	0,00014922
			RMSE_X =	0,02109646			RMSE_Y =	0,01922489			RMSE_Z =	0,01601813

RMSE_XY = 0,02854219
RMSE_XYZ = 0,03272976

APA's 2022 survey presents the smaller RMSE for all coordinates, especially for the Z coordinate. If we compare APA's 2022 survey with ours (processed with Agisoft Metashape and WebODM), and consider the altimetric precision, the RMSE_XYZ

outperforms the Agisoft Metashape and WebODM results by a factor of 9 and 19 respectively.

The RMSE calculated for the dataset processed without GCPs is the largest for all coordinates by at least a factor of 10, with the altimetric accuracy having an error of more than 6 meters.

Table 8. Calculated RMSE for our own survey, processed with WebODM, without GCPs. The real values were obtained from the 2021 APA survey.

Check Point	**X coordinates**				**Y coordinates**				**Z coordinates**			
	Real	Obtained	Residual X	Residual X^2	Real	Obtained	Residual Y	Residual Y^2	Real	Obtained	Residual Z	Residual Z^2
1	-54348,4242	No data	No data	No data	195928,7281	No data	No data	No data	10,0594	No data	No data	No data
2	-54364,1133	-54363,9252	-0,1881	0,03538578	195922,2108	195922,7875	-0,5766	0,33251330	10,0218	15,9800	-5,9582	35,49982309
3	-54348,9393	-54348,7019	-0,2374	0,05634394	195908,4483	195909,0262	-0,5779	0,33401981	10,1960	16,5600	-6,3640	40,50080354
4	-54380,2926	-54380,1541	-0,1385	0,01916962	195883,0576	195883,4832	-0,4257	0,18118169	9,5550	15,9700	-6,4150	41,15160050
5	-54301,9266	-54301,5162	-0,4104	0,16845488	195876,4610	195876,6982	-0,2372	0,05627016	8,6893	15,6200	-6,9307	48,03419688
6	-54289,2387	-54288,6527	-0,5860	0,34338807	195931,6649	195932,2290	-0,5642	0,31828029	6,8395	13,1431	-6,3036	39,73537087
7	-54378,5469	-54378,5204	-0,0264	0,00069921	196017,1264	196018,0101	-0,8838	0,78104931	9,5954	16,7770	-7,1816	51,57581139
8	-54294,5253	-54293,8187	-0,7066	0,49932482	196022,6532	196023,6569	-1,0037	1,00747618	5,5605	11,8300	-6,2695	39,30724930
9	-54241,6293	-54240,5594	-1,0699	1,14469730	196193,5093	196195,6263	-2,1170	4,48167815	5,6927	12,0691	-6,3763	40,65762555
10	-54211,6193	-54210,2306	-1,3887	1,92841833	196308,5090	196311,1032	-2,5942	6,72994418	5,1962	12,0400	-6,8438	46,83697933
11	-54239,3079	-54238,0279	-1,2800	1,63834178	196306,3845	196308,8563	-2,4718	6,10995631	5,1750	12,2100	-7,0350	49,49154489
12	-54357,2679	-54356,8066	-0,4613	0,21280073	196046,5520	196047,7649	-1,2129	1,47116826	9,6147	15,6200	-6,0053	36,06306165
			RMSE_X =	0,74143745			RMSE_Y =	1,40788486			RMSE_Z =	6,52863669

RMSE_XY =	1,59118487
RMSE_XYZ =	6,71974451

The same procedure was used to calculate the RMSE for all the remaining orthophotomaps. The results[3] can be seen in table 9.

Table 9. Calculated RMSE for all orthophotomaps

RMSE												
Orthophotomap	**Check Points (m)**						**GCPs (values from software reports)**					
	# of check points	X	Y	Z	XY	XYZ	# of GCPs	X	Y	Z	XY	XYZ
APA 2021 (Pix4D)	-	0,00000000	0,00000000	0,00000000	0,00000000	0,00000000	9	0,01374444	0,02851111	0,05622222	0,03175556	-
APA 2021 (Agisoft)	12	0,01970745	0,02409964	0,05954004	0,03113160	0,06718774	5	0,01817710	0,01521250	0,01821200	0,02370290	0,02989150
APA 2021 (WebODM)	12	0,05837724	0,06637846	0,13490379	0,08839684	0,16128557	5	0,01600000	0,00200000	0,02700000	-	0,01800000
APA 2022 (Pix4D)	12	0,02109646	0,01922489	0,01601813	0,02854219	0,03272976	9	-	-	-	0,02700000	-
APA 2022 (Agisoft)	12	0,01932141	0,02904143	0,07608491	0,03488154	0,08369967	5	0,01252190	0,01498930	0,01220590	0,01953140	0,02303170
APA 2022 (WebODM)	12	0,04212994	0,05435181	0,13427884	0,06876809	0,15086370	5	0,00200000	0,00300000	0,00300000	-	0,00200000
Own (Agisoft)	11	0,07029830	0,06064845	0,27274553	0,09284441	0,28811492	4	0,01358690	0,01119230	0,00624480	0,01760320	0,01867810
Own (WebODM)	10	0,05084286	0,05758513	0,61390922	0,07681825	0,61869667	4	0,01000000	0,01000000	0,06000000	-	0,04000000
Own (WebODM, without GCPs)	11	0,74143745	1,40788486	6,52863669	1,59118487	6,71974451	0	-	-	-	-	-

These results suggest that, for now, GCPs are still essential for the planimetric accuracy of orthophotomaps and altemetric precision needs to be particularly assessed. For this sample, a conclusion that Pix4D and Agisoft Metashape have a better altimetric accuracy than WebODM can also be drawn.

---

[3] APA's survey of the Aguçadoura region was divided into two sections. The RMSE values for the 2021 dataset processed with Pix4D were averaged from the values of both reports (one with 4 GCPs, the other with 5). For the 2022 dataset only a final report was available.

For the rest of this section the results of DSMs differences and the fusion process will be assessed. In all raster operations where more than one raster image is being used, the result was downsampled (the dataset with the largest pixel size was used as reference). The reason for this is the attempt to minimize the noise that can occur when upsampling images.

Figures 38 and 39 show the DSMs generated from APA's datasets collected in 2022 and 2021, respectively. The result of a raster difference operation is presented in figure 40. The resulting raster shows the differences between the two DSMs, representing two different epochs. This corresponds to the changes that occurred between the two time periods. In this case, with the exception of the sandy area next to the water, almost no change is observed (yellow represents no change) and the extreme values (with the exception of the watercourse, where reflectance can be challenging to assess) occur in the vicinity of built structures, for the reasons previously presented (see figure 33).

Figure 38 – DSM, APA 2022 (Pix4D), pixel size: 0,015x0,015 m

Figure 39 – DSM, APA 2021 (Pix4D), pixel size: 0,05x0,05m

Figure 40 – Difference of DSMs (2022 DSM – 2021 DSM), pixel size: 0,05x0,05m

The DSMs generated from our UAV survey were also used to perform the same raster difference operation. Figures 41 through 46 show the results of this operation. Once more, the extreme values occur essentially around buildings.

Figure 41 – DSM, 2022 (Agisoft), pixel size: 0,083x0,083m
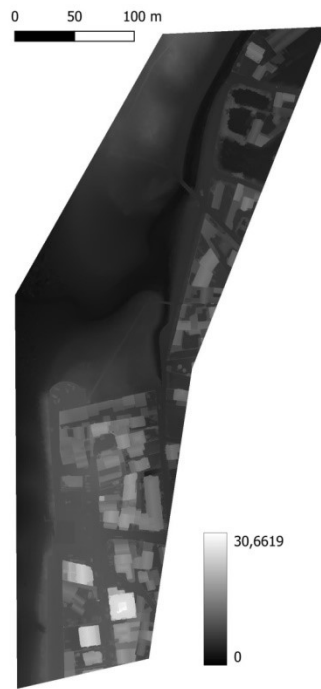
Figure 42 – DSM, APA 2021 (Pix4D), pixel size: 0,05x0,05m

Figure 43 – Difference of DSMs (2022–2021), pixel size: 0,083x0,083m
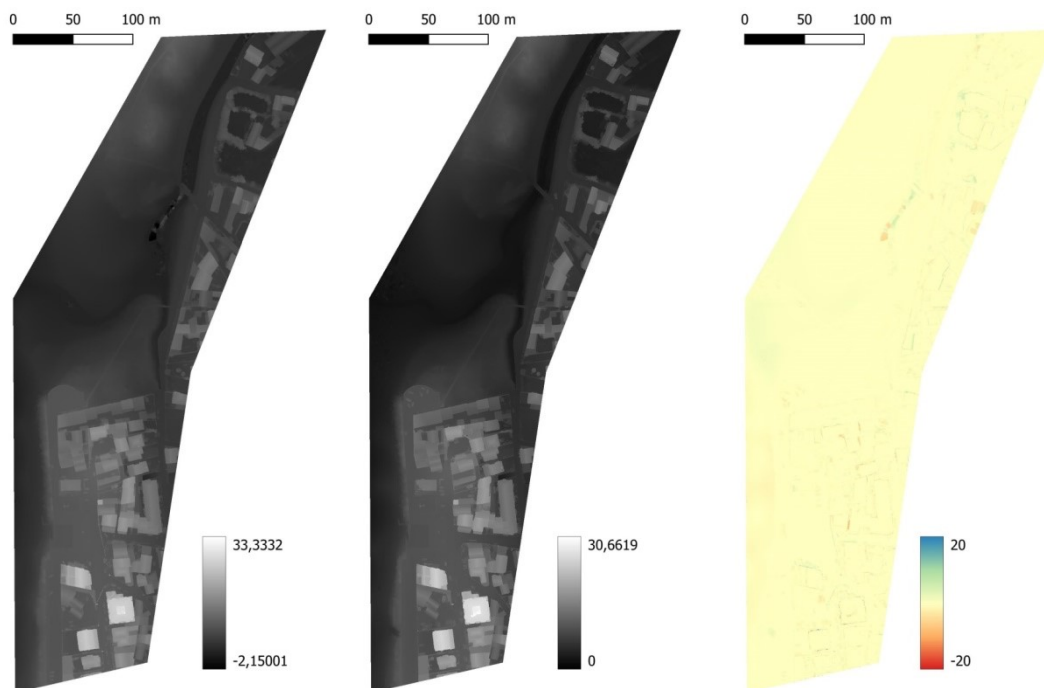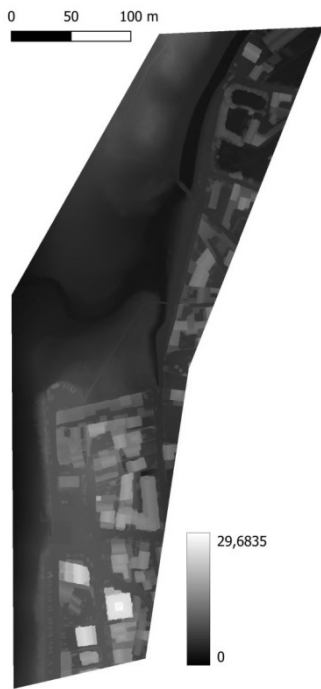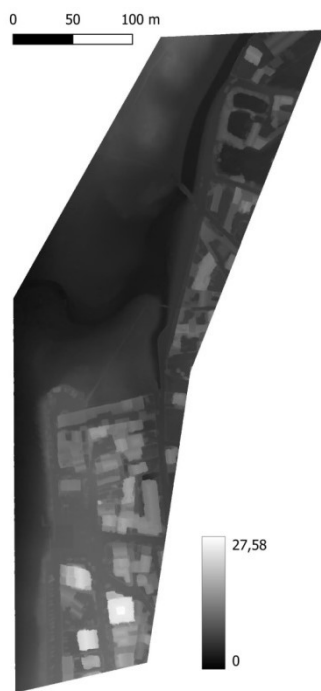

Figure 44 – DSM, WebODM (2022), pixel size: 0,076x0,076m
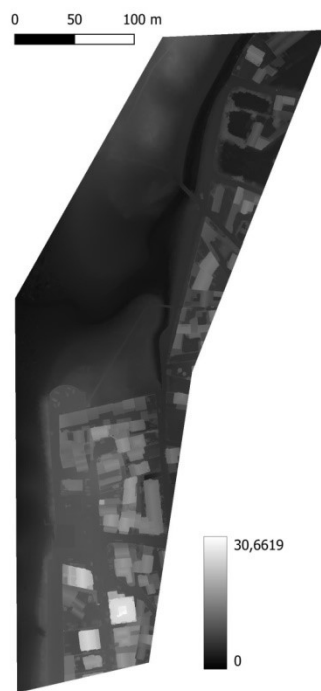
Figure 45 – DSM, APA 2021 (Pix4D), pixel size: 0,05x0,05m

Figure 46 – Difference of DSMs (2022–2021), pixel size: 0,076x0,076m

Having previously determined the RMSE for all datasets in order to establish the altimetric accuracy, a comparison of the differences between DSMs was

performed. The results of a raster difference of "raster differences" can be seen in figures 47 to 49. We used the pairs with lower RMSE.
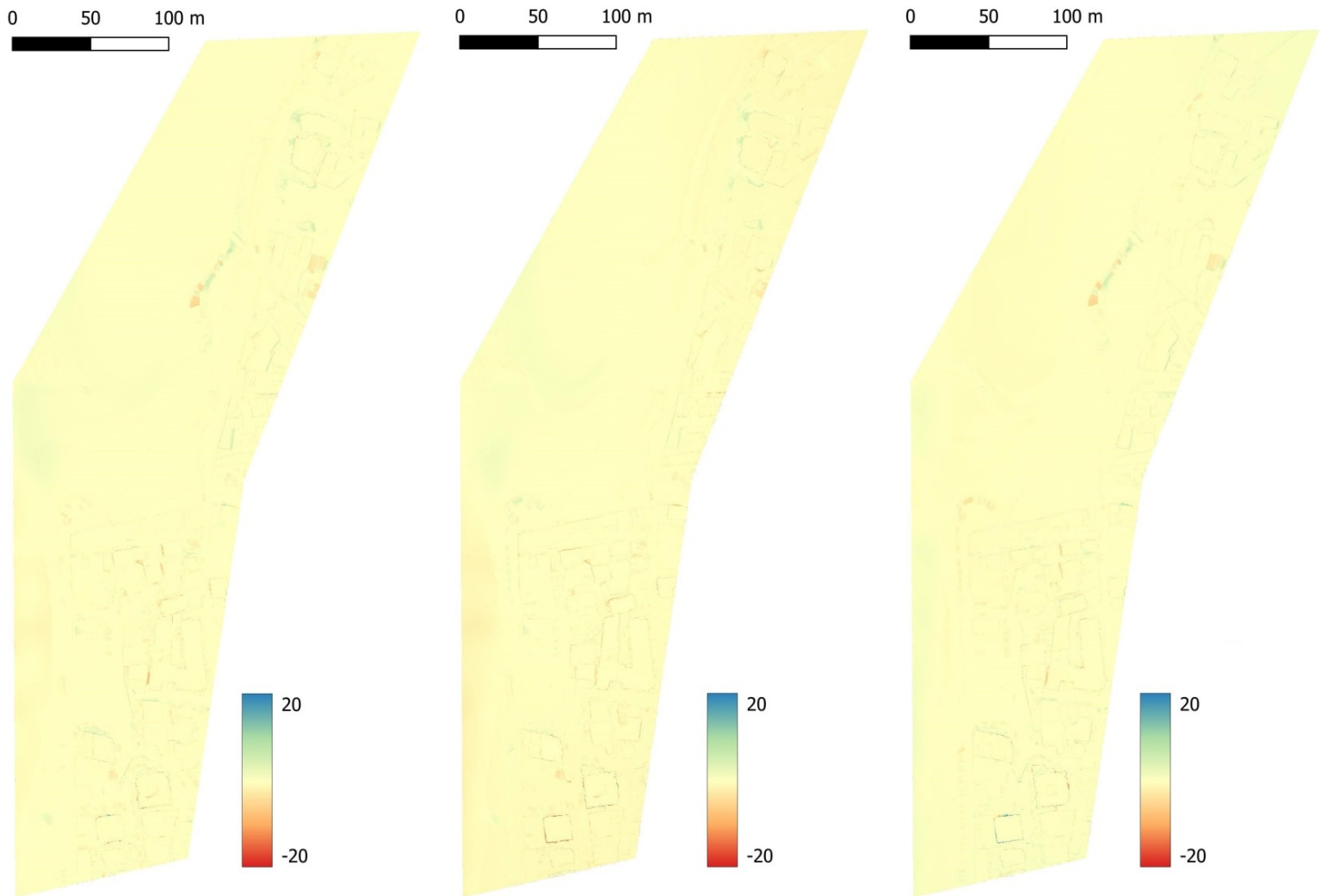
Figure 47 – Difference of DSMs (APA 2022 – APA 2021), pixel size: 0,05x0,05m

Figure 48 – Difference of DSMs (Agisoft 2022– APA 2021), pixel size: 0,083x0,083m

Figure 49 – Difference of "difference of DSMs", pixel size: 0,083x0,083m

The product of this operation (figure 49) shows that the differences are zero, or near zero, for most of the raster (yellow represents the value zero), except on the edges of buildings and on the water course, where reflectance can be challenging to assess. What this result suggests is that the two datasets correlate well and – taking in consideration the edges of buildings and the water courses – either one could be used to assess the changes that occurred between both time periods.

A comparison between the datasets from our UAV survey was also performed. The DSMs generated with Agisoft Metashape and WebODM were compared. Figures 50 to 52 show the result.
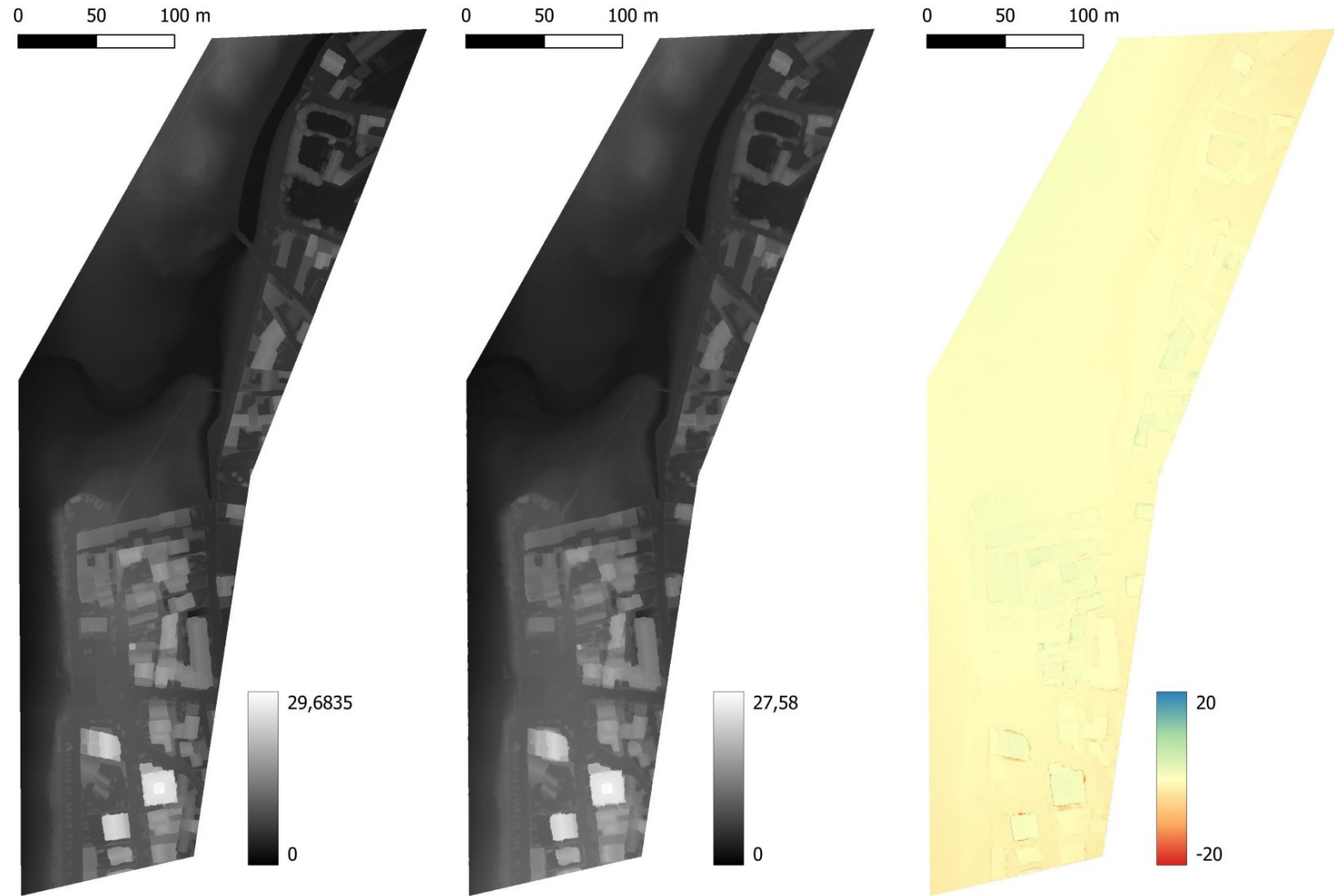
Figure 50 –DSM, Agisoft 2022, pixel size:

Figure 51 – DSM, ODM 2022, pixel size:

Figure 52 – Difference of DSMs, pixel size:

As seen in table 9, WebODM performed worse than Agisoft Metashape, especially for altimetric accuracy. As shown in figure 52, there are some differences within and around the built-up areas (top right, bottom). Since the datasets are the same, these differences are related to the choice of processing algorithms. Some fine-tuning is necessary to adjust the best processing algorithm to the data.

In the last part of this section the fusion process (pixel level) will be analysed.

As mentioned before, the objective of fusing different datasets is to obtain a final product with more information than any of the sources.

To assess the potentialities of data fusion the NDVI index (a well-established index in CD) was firstly calculated for the Sentinel 2 datasets (2021 and 2022) and a difference of rasters was performed (result shown in figure 55).

Figure 53 – NDVI index, Sentinel 2 images, pixel size : 10x10m, 06/02/2022
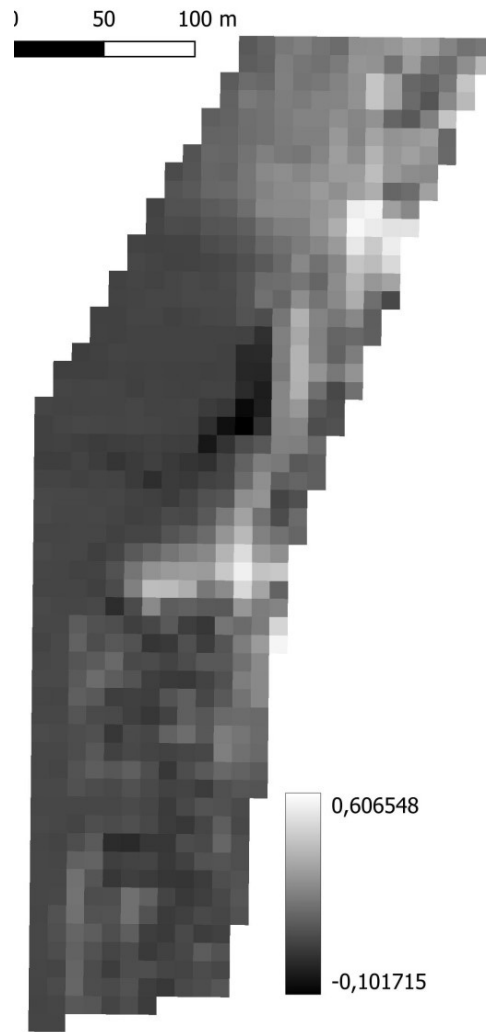
Figure 54 – NDVI index, Sentinel 2 images, pixel size : 10x10m, 28/02/2021

Figure 55 – difference of NDVI's (2022 NDVI – 2021 NDVI), pixel size: 10x10m

Figure 55 conveys the information (changes in NDVI index) that can be extracted from the Sentinel 2 datasets. The pixel size of the final product is 10x10m.

Next, Sentinel 2 datasets were fused with datasets that have a much greater spatial resolution (APA 2021, Pix4D, pixel size: 0,025x0,025m and our UAV survey, Agisoft Metashape, pixel size: 0,041x0,041m).

The results of this operation can be seen in figures 56 to 58.
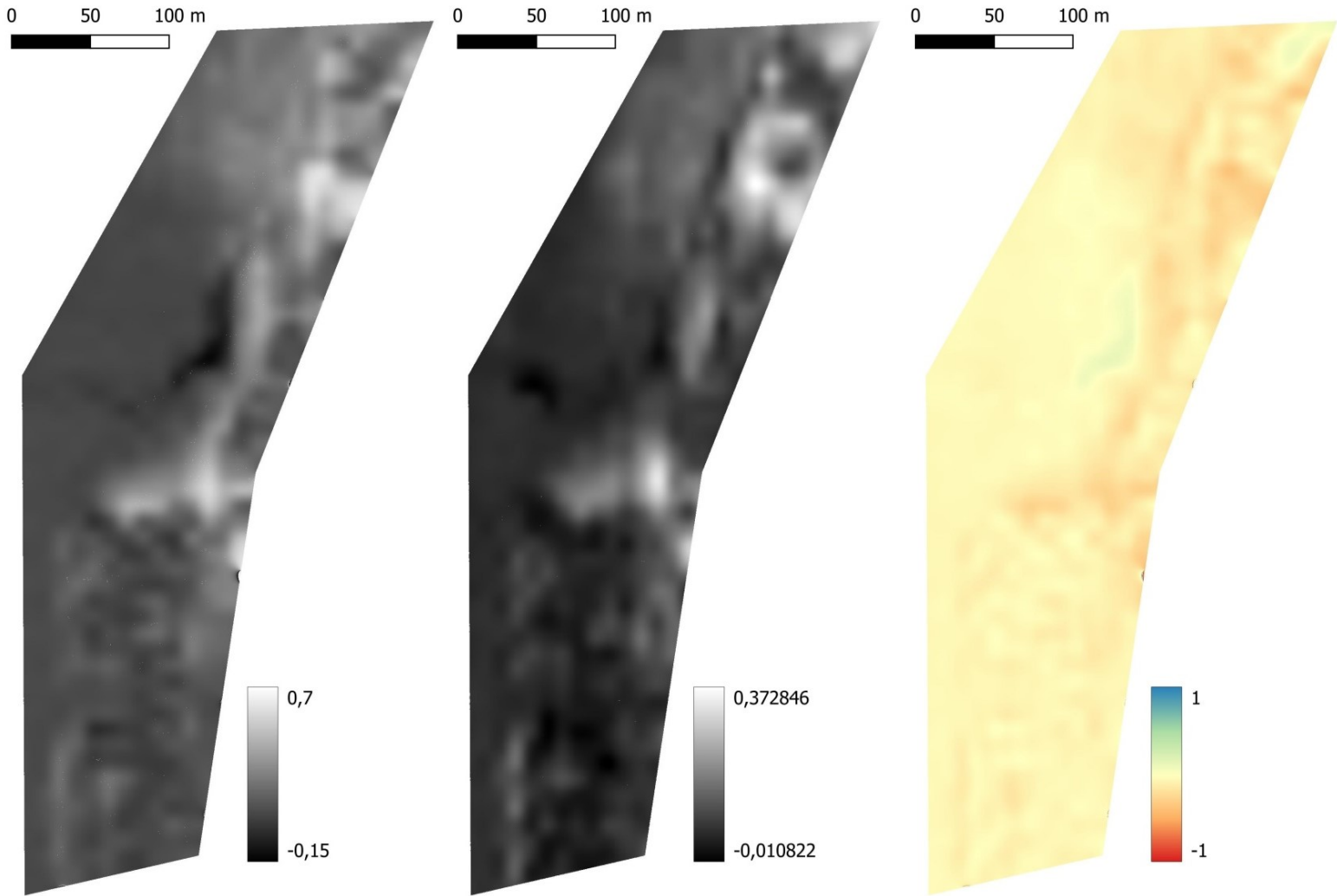
Figure 56 – NDVI index from fused dataset (APA and satellite, 2021), pixel size: 0,025x0.025m

Figure 57 – NDVI index from fused dataset (Agisoft and satellite, 2022), pixel size: 0,041x0,041m

Figure 58 – difference of NDVI's (2022 NDVI – 2021 NDVI), pixel size: 0,041x0,041m

From a direct comparison of figures 53 to 58 the difference in detail is evident. The fused products have a much higher level of detail, but attention needs to be paid when examining the results. Since the difference in spatial scales is a few orders of magnitude, the original pixels have a much coarser classification. This means that a considerable percentage of pixels in the fused image (with much higher spatial resolution) may be misclassified. The result continues to be more informative than the original satellite data, but accuracy should be assessed with some care.

The results presented in this section will be discussed in section 5.

5. DISCUSSION

The RMSE values (see table 9) are a clear indication of the importance of using GCPs. The orthophotomap generated from our own survey, without GCPs, presents very significant errors for all check points. But even when GCPs were used, there are significant differences between the RMSE that the software presented for the GCPs and the RMSE calculated for the check points.

Sanz-Ablanedo et al. (2018) addressed this issue, noting that SfM models adapt to the GCPs coordinates using similar weights for all axes. "When RMSE is calculated for the control points, there is no difference between the three components, as the deformation of the model adapts to the control points using the same weight for the three axes. However, when RMSEs are calculated for the check points with the same combinations, a greater variation between the vertical and horizontal axes can be detected clearly". [6, p. 11]

This effect is observed in all of the processed orthophotomaps and corroborates that it "is not possible to correctly evaluate the geometric quality of an SfM 3D model using just a few check points, and indeed it can be perilous. (…). Consequently, a good evaluation of the geometric quality of an SfM 3D model should include many check points, which must be also evenly distributed across the whole area and not just located at the periphery". [6, p. 15]

This recommendation was implemented as far as possible, since in the beach area there were not enough unique features to be used as check points. Twelve check points were chosen to complement the five GCPs and this should give a fairly precise indication of the RMSE for the entire model.

Sanz-Ablanedo et al. (2018) noted how "it is not possible to achieve a vertical accuracy that approaches the GSD, regardless of the number of GCPs used in a project. For plan accuracy, it is possible to achieve an accuracy similar to the GSD, providing there is at least one GCP for 35 images (…). In practice, this represents a very high number of GCPs. With a more modest 50 images per GCP, a vertical accuracy of 2 × GSD and a 1.2 × GSD horizontal accuracy is achieved. With 75 images per GCP,

accuracy worsens to 3 × GSD for vertical accuracy and 2 × GSD for horizontal accuracy". [6, p. 16]

The results obtained, with the exception of the orthophotomaps processed with WebODM, seem to agree with Sanz-Ablanedo et al. (2018) findings.

"If few GCPs are used, the RMSE in check points will be about ±5 times the averaged GSD of the project. By introducing a higher number of GCPs (more than 2 GCPs per 100 photos in our case study) the RMSE will converge slowly to a value approximately double the average GSD. These values are valid in 3D. As in classical photogrammetry, vertical errors in SfM photogrammetry will be 2.5 times the error of easting or northing components. The study has demonstrated that GCPs should be evenly distributed around the whole interest area, ideally in a triangular mesh grid, since with this setup the maximum distance to any GCP is minimized. Results indicate that for a given number of GCP, the accuracy achieved using an optimal distribution will be twice as good as that if GCPs are poorly distributed". [6, p. 17]

Sanz-Ablanedo et al. (2018) gave a recommendation for situations where check points are not available.

"Accuracy should not be measured using the ground points used to control the BA. However, if independent check points are not available, real accuracy could be estimated by multiplying the 3D-RMSE derived from the GCP by a factor of 3 if the project has a high (more than 3.5 GCPs per 100 photos in our case study) or 4–8 if the project has a low number of GCPs (less than 2 GCPs per 100 photos)". [6, p. 17]

According to ASPRS 2014 standards, the RMSE obtained for the processed orthophotomaps, with exception of the case where no GCPs were used, places them in the category of High Accuracy Digital Planimetric Data, with map scales varying from 1:200 to 1:400.

The differences of rasters performed in section 4 revealed some extreme values around the buildings and on the water surface. As mentioned, the errors around buildings are a result of the algorithms used in the SfM method. The choice of the best

algorithm is not straightforward and requires fine-tuning and compromises to obtain the best result for each case.

Koeva et al. (2018) noted how the quality of the orthophotomaps "depends on which algorithm is used to interpolate the DSM from the point cloud. A common method is triangulation, which may result in noise around overhanging roof edges (…). Other interpolation methods, such as Inverse Distance Weighting, improve the visual appearance of overhanging roofedges, but cause rounded roofcorners (…). Such observations stress that quality of the DSM and orthophoto also depend on which software and algorithms are utilised". [2, p. 322]

The erros on the water surface are related to its reflectance. Caroti et al. (2017) reported a problem with the camera's automatic focus caused by this issue.

"Water surface is in fact too homogeneous for automatic focusing to work correctly, which caused blurred images in some cases and image skipping in others. This problem has been solved by setting manual focus at infinity, as the flight level was greater than the hyperfocal distance". [44, p. 6]

In terms of the fusion process, one of the principal issues is the discrepancy in spatial scales of the source images. Images with pixel sizes of a few centimetres were fused with satellite images with a pixel size of 10 meters.

Zhang (2010) addressed this issue, referring the need for new fusion methods.

"For example, for a pair of PAN and MS images with very high resolution, one pixel in the MS image corresponds to several pixels from variant spectral features observable in the PAN band. The resolution transition from low to high or very high therefore leads to new demands for pan-sharpening techniques. Thus, one of the trends for pan-sharpening techniques is to develop new methods for dealing with high-resolution images. For the fusion of SAR and optical images, or LiDAR intensity images, however, higher resolution leads to more difficulties in co-registration of these images." [7, p. 17]

However, even with the difficulties that still affect pixel-level fusion, Li et al. (2017) concluded that it is "one of the most important techniques to integrate and analyze information from multiple sources". [30, p. 110]

The results obtained (figures 53 to 58) suggest the potential of this technique. Spectral information originally only available with a pixel size of 10 meters is now available with a pixel size of a few centimetres. Taking into account the aforementioned problems, such as the much greater spectral variation of high resolution images, the end result conveys more spectral information than the original satellite image.

FINAL REMARKS

Throughout this work, we sought to evaluate the accuracy of UAVs' RS data and its potential for updating Geoinformation. The results obtained in section 4, and discussed in section 5, suggest that not only UAVs' RS data are suitable for updating Geoinformation, but they are capable of achieving great detail with high accuracy.

Even the orthophotomap processed without GCPs obtained an arguably small RMSE_XY of 1,6 meters. This type of error suggests that the orthophotomap generated might be used in situations where a submeter planimetric accuracy is not needed.

However, several 'uncertainties' are present in all the resulting products. Many factors contributed to these errors. For example, the sensors that were used were different. APA 2021 and APA 2022 surveys used different RGB cameras, with different resolutions. Our survey also used a different camera, with a lower resolution than the two APA cameras. This factor alone implies significant differences in the resulting orthophotomaps.

Another reason for uncertainty is the choice of software/algorithms. Computing power and time constraints meant that extensive comparative analysis of software and processing algorithms was not carried out. Many processing parameters were not fine-tuned and default values were used; an example of this is the downsampling that occurred in some orthophotomaps, where the pixel size is bigger than the GSD.

Many other factors contributed to the errors present in the final products: weather conditions, time of day (lighting and shadow conditions), UAVs used, arrangement of GCPs, etc.

Despite all the 'uncertainties', some of the results obtained seem to agree with the findings of Sanz-Ablanedo et al. (2018). Check points in APA's surveys, processed with Agisoft Metashape, have a 3D RMSE that is three times higher than GCPs. The same is not true for the remaining orthophotomaps. This occurred because APA's surveys used cameras with higher resolution than ours and Agisoft Metashape seems to perform better with the collected data.

The fused products also present some uncertainties. As Zhang (2010) noted, "the techniques remain challenging for multi-source data fusion within varying spatial and temporal resolutions". [7, p. 5]

The final products, despite showing a promising potential and being an improvement in relation to the original spectral information, need further investigation. Fusion with RS data with a bigger spatial resolution, as well as fusion at the feature and decision level, needs to be compared in order to establish the most effective technique for our research problem.

Assessing the true accuracy of the fused products requires a comprehensive statistical analysis, which is beyond the scope of this work.

However, this dissertation is the starting point for a more profound research that will be carried on in our doctoral thesis. That investigation aims to assess the relevance and performance of data obtained by UAVs in updating large-scale Geoinformation. All the issues and limitations of this work will be addressed in that future research.

BIBLIOGRAPHY

[1]   C. Gevaert, C. Persello, S. O. Elberink, G. Vosselman, and R. Sliuzas, "An automated technique for basemap updating using UAV data," in *2017 Joint Urban Remote Sensing Event, JURSE 2017*, 2017.

[2]   M. Koeva, M. Muneza, C. Gevaert, M. Gerke, and F. Nex, "Using UAVs for map creation and updating. A case study in Rwanda," *Surv. Rev.*, vol. 50, no. 361, pp. 312–325, 2018.

[3]   T. Adão *et al.*, "Hyperspectral imaging: A review on UAV-based sensors, data processing and applications for agriculture and forestry," *Remote Sens.*, vol. 9, no. 11, 2017.

[4]   H. Yao, R. Qin, and X. Chen, "Unmanned aerial vehicle for remote sensing applications - A review," *Remote Sens.*, vol. 11, no. 12, pp. 1–22, 2019.

[5]   N. Haala, M. Cramer, and M. Rothermel, "Quality of 3D Point Clouds From Highly Overlapping Uav Imagery," *ISPRS - Int. Arch. Photogramm. Remote Sens. Spat. Inf. Sci.*, vol. XL-1/W2, no. April 2015, pp. 183–188, 2013.

[6]   E. Sanz-Ablanedo, J. H. Chandler, J. R. Rodríguez-Pérez, and C. Ordóñez, "Accuracy of Unmanned Aerial Vehicle (UAV) and SfM photogrammetry survey as a function of the number and location of ground control points used," *Remote Sens.*, vol. 10, no. 10, 2018.

[7]   J. Zhang, "Multi-source remote sensing data fusion: Status and trends," *Int. J. Image Data Fusion*, vol. 1, no. 1, pp. 5–24, 2010.

[8]   L. Bai, C. Xu, and C. Wang, "A review of fusion methods of multi-spectral image," *Optik (Stuttg).*, vol. 126, no. 24, pp. 4804–4807, 2015.

[9]   A. P. Tewkesbury, A. J. Comber, N. J. Tate, A. Lamb, and P. F. Fisher, "A critical synthesis of remotely sensed optical image change detection techniques," *Remote Sens. Environ.*, vol. 160, pp. 1–14, 2015.

[10]   L. Negash, H.-Y. Kim, and H.-L. Choi, "Emerging UAV Applications in Agriculture," in *2019 7th International Conference on Robot Intelligence Technology and*

Applications, RiTA 2019, 2019, pp. 254–257.

[11]   N. E. Kolarik *et al.*, "A multi-plot assessment of vegetation structure using a micro-unmanned aerial system (UAS) in a semi-arid savanna environment," *ISPRS J. Photogramm. Remote Sens.*, vol. 164, pp. 84–96, Jun. 2020.

[12]   F. Mancini, M. Dubbini, M. Gattelli, F. Stecchi, S. Fabbri, and G. Gabbianelli, "Using unmanned aerial vehicles (UAV) for high-resolution reconstruction of topography: The structure from motion approach on coastal environments," *Remote Sens.*, vol. 5, no. 12, pp. 6880–6898, 2013.

[13]   M. J. Westoby, J. Brasington, N. F. Glasser, M. J. Hambrey, and J. M. Reynolds, "'Structure-from-Motion' photogrammetry: A low-cost, effective tool for geoscience applications," *Geomorphology*, vol. 179, pp. 300–314, 2012.

[14]   J. F. Reinoso, J. E. Gonçalves, C. Pereira, and T. Bleninger, "Cartography for Civil Engineering Projects: Photogrammetry Supported by Unmanned Aerial Vehicles," *Iran. J. Sci. Technol. - Trans. Civ. Eng.*, vol. 42, no. 1, pp. 91–96, 2018.

[15]   M. A. Fonstad, J. T. Dietrich, B. C. Courville, J. L. Jensen, and P. E. Carbonneau, "Topographic structure from motion: A new development in photogrammetric measurement," *Earth Surf. Process. Landforms*, vol. 38, no. 4, pp. 421–430, 2013.

[16]   M. W. Smith, J. L. Carrivick, and D. J. Quincey, "Structure from motion photogrammetry in physical geography," *Prog. Phys. Geogr.*, vol. 40, no. 2, pp. 247–275, 2016.

[17]   K. Nikolakopoulos *et al.*, "Preliminary results from active landslide monitoring using multidisciplinary surveys," *Eur. J. Remote Sens.*, vol. 50, no. 1, pp. 280–299, 2017.

[18]   S. Jayathunga, T. Owari, S. Tsuyuki, and Y. Hirata, "Potential of UAV photogrammetry for characterization of forest canopy structure in uneven-aged mixed conifer–broadleaf forests," *Int. J. Remote Sens.*, vol. 41, no. 1, pp. 53–73, Jan. 2020.

[19]   C. H. Grohmann, G. P. B. Garcia, A. A. Affonso, and R. W. Albuquerque, "Dune

migration and volume change from airborne LiDAR, terrestrial LiDAR and Structure from Motion-Multi View Stereo," *Comput. Geosci.*, vol. 143, no. March, p. 104569, 2020.

[20] Á. Gómez-Gutiérrez and G. R. Gonçalves, "Surveying coastal cliffs using two UAV platforms (multirotor and fixed-wing) and three different approaches for the estimation of volumetric changes," *Int. J. Remote Sens.*, vol. 41, no. 21, pp. 8143–8175, 2020.

[21] J. N. Callow, S. M. May, and M. Leopold, "Drone photogrammetry and KMeans point cloud filtering to create high resolution topographic and inundation models of coastal sediment archives," *Earth Surf. Process. Landforms*, vol. 43, no. 12, pp. 2603–2615, 2018.

[22] P. Surovỳ and K. Kuželka, "Acquisition of forest attributes for decision support at the forest enterprise level using remote-sensing techniques-a review," *Forests*, vol. 10, no. 3. MDPI AG, 2019.

[23] K. B. Dang, V. B. Dang, Q. T. Bui, V. V. Nguyen, T. P. N. Pham, and V. L. Ngo, "A Convolutional Neural Network for Coastal Classification Based on ALOS and NOAA Satellite Data," *IEEE Access*, vol. 8, pp. 11824–11839, 2020.

[24] A. Gebrehiwot, L. Hashemi-Beni, G. Thompson, P. Kordjamshidi, and T. E. Langan, "Deep convolutional neural network for flood extent mapping using unmanned aerial vehicles data," *Sensors (Switzerland)*, vol. 19, no. 7, Apr. 2019.

[25] H. Ghassemian, "A review of remote sensing image fusion methods," *Inf. Fusion*, vol. 32, pp. 75–89, 2016.

[26] N. Joshi *et al.*, "A review of the application of optical and radar remote sensing data fusion to land use mapping and monitoring," *Remote Sens.*, vol. 8, no. 1, p. 70, Jan. 2016.

[27] R. Dian, S. Li, L. Fang, and Q. Wei, "Multispectral and hyperspectral image fusion with spatial-spectral sparse representation," *Inf. Fusion*, vol. 49, no. November 2018, pp. 262–270, 2019.

[28] D. E. Nirmala and V. Vaidehi, "Comparison of pixel-level and feature level image

fusion methods," *2015 Int. Conf. Comput. Sustain. Glob. Dev. INDIACom 2015*, pp. 743–748, 2015.

[29] H. Tian and B. Wang, "Discussion and analyze on image fusion technology," in *2009 2nd International Conference on Machine Vision, ICMV 2009*, 2009, pp. 246–250.

[30] S. Li, X. Kang, L. Fang, J. Hu, and H. Yin, "Pixel-level image fusion: A survey of the state of the art," *Inf. Fusion*, vol. 33, pp. 100–112, 2017.

[31] U. Andriolo, G. Gonçalves, F. Bessa, and P. Sobral, "Mapping marine litter on coastal dunes with unmanned aerial systems: A showcase on the Atlantic Coast," *Sci. Total Environ.*, vol. 736, 2020.

[32] R. Qin, J. Tian, and P. Reinartz, "3D change detection – Approaches and applications," *ISPRS J. Photogramm. Remote Sens.*, vol. 122, pp. 41–56, 2016.

[33] C. Gómez, J. C. White, and M. A. Wulder, "Optical remotely sensed time series data for land cover classification: A review," *ISPRS J. Photogramm. Remote Sens.*, vol. 116, pp. 55–72, 2016.

[34] R. F. de Deus and J. A. Tenedório, "Coastal Land-Use and Land-Cover Change Trajectories: Are They Sustainable?," *Sustain. 2021, Vol. 13, Page 8840*, vol. 13, no. 16, p. 8840, Aug. 2021.

[35] C. D. Lloyd, *Exploring Spatial Scale in Geography*. 2013.

[36] B. Jiang and S. Anders Brandt, "A Fractal Perspective on Scale in Geography," *ISPRS Int. J. Geo-Information*, vol. 5, no. 6, 2016.

[37] H. Couclelis, "The certainty of uncertainty: GIS and the limits of geographic knowledge," *Trans. GIS*, vol. 7, no. 2, pp. 165–175, 2003.

[38] G. Fusco, M. Caglioni, K. Emsellem, M. Merad, D. Moreno, and C. Voiron-Canicio, "Questions of uncertainty in geography," *Environ. Plan. A*, vol. 49, no. 10, pp. 2261–2280, 2017.

[39] A. Comber, P. Fisher, and A. Brown, "Uncertainty, vagueness and indiscernibility: the impact of spatial scale in relation to the landscape elements," 2007.

[40]   L. R. Alves Júnior, M. E. Ferreira, J. B. R. Côrtes, and L. A. de Castro Jorge, "High accuracy mapping with cartographic assessment for a fixed-wing remotely piloted aircraft system," *J. Appl. Remote Sens.*, vol. 12, no. 01, p. 1, 2018.

[41]   M. Daakir, Y. Zhou, M. Pierrot Deseilligny, C. Thom, O. Martin, and E. Rupnik, "Improvement of photogrammetric accuracy by modeling and correcting the thermal effect on camera calibration," *ISPRS J. Photogramm. Remote Sens.*, vol. 148, no. January 2018, pp. 142–155, 2019.

[42]   M. Hussain, D. Chen, A. Cheng, H. Wei, and D. Stanley, "Change detection from remotely sensed images: From pixel-based to object-based approaches," *ISPRS J. Photogramm. Remote Sens.*, vol. 80, pp. 91–106, 2013.

[43]   W. Wang, M. Hall-Beyer, C. Wu, W. Fang, and W. Nsengiyumva, "Uncertainty problems in image change detection," *Sustain.*, vol. 12, no. 1, 2020.

[44]   G. Caroti, A. Piemonte, and R. Nespoli, "UAV-Borne photogrammetry: A low cost 3D surveying methodology for cartographic update," *MATEC Web Conf.*, vol. 120, pp. 1–10, 2017.

ANNEXES

ODM Quality Report

Dataset Summary

Date	12/07/2022 at 17:49:47
Area Covered	0.191596 km²
Processing Time	27.0m:23.0s
Capture Start	26/03/2022 at 14:42:56
Capture End	26/03/2022 at 15:02:17

Processing Summary

Reconstructed Images	88 over 88 shots (100.0%)
Reconstructed Points (Sparse)	141813 over 145459 points (97.5%)
Reconstructed Points (Dense)	10,544,227 points
Average Ground Sampling Distance (GSD)	4.2 cm
Detected Features	13,144 features
Reconstructed Features	5,148 features
Geographic Reference	GPS and GCP
GPS / GCP errors	6.29 / 0.00 meters
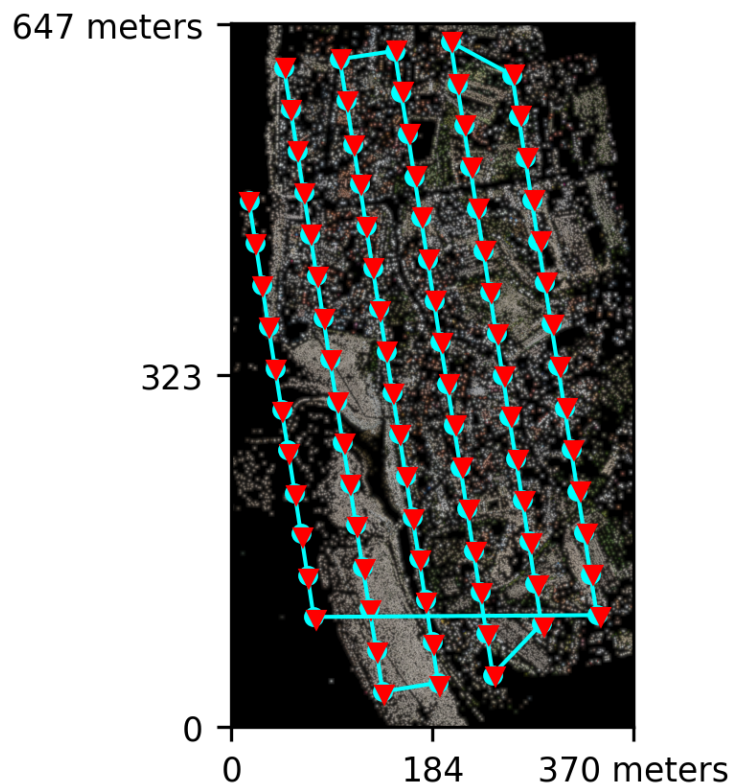
Previews

Orthophoto
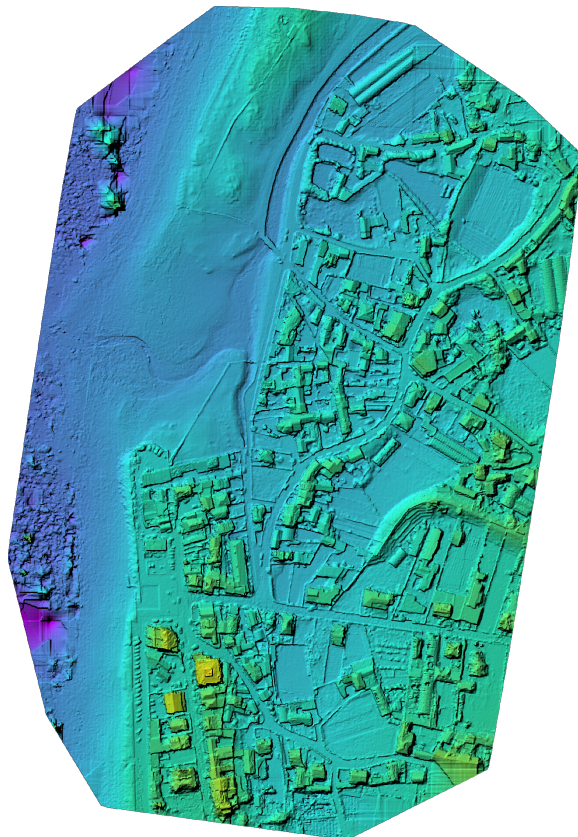
Digital Surface Model

-9.94m   27.63m

Digital Terrain Model

-11.29m   19.99m

Survey Data

2 ■ 3 ■ 4 ■ 5+

GPS/GCP/3D Errors Details

GPS	Mean	Sigma	RMS Error
X Error (meters)	-1.979	0.634	2.078
Y Error (meters)	-0.867	0.870	1.228
Z Error (meters)	-5.789	1.205	5.913
Total			6.286

GCP	Mean	Sigma	RMS Error
X Error (meters)	-0.000	0.001	0.001
Y Error (meters)	-0.001	0.001	0.001
Z Error (meters)	0.003	0.006	0.006
Total			0.004

3D	Mean	Sigma	RMS Error
X Error (meters)	0.013	0.015	0.020
Y Error (meters)	0.012	0.014	0.018
Z Error (meters)	0.026	0.039	0.047
Total			0.035

	Absolute	Relative
Horizontal Accuracy CE90 (meters)	0.003	0.038
Vertical Accuracy LE90 (meters)	0.013	0.063

Ground Control Point Error

ID	Error X (m)	Error Y (m)	Error Z (m)
GCP-0	-0.000	0.000	-0.000
GCP-1	-0.002	-0.003	0.013
GCP-2	0.001	0.000	-0.001
GCP-3	-0.000	0.000	0.000

Features Details

Detected features heatmap for camera v2 dji fc3170 4000 2250 brown 0.6666
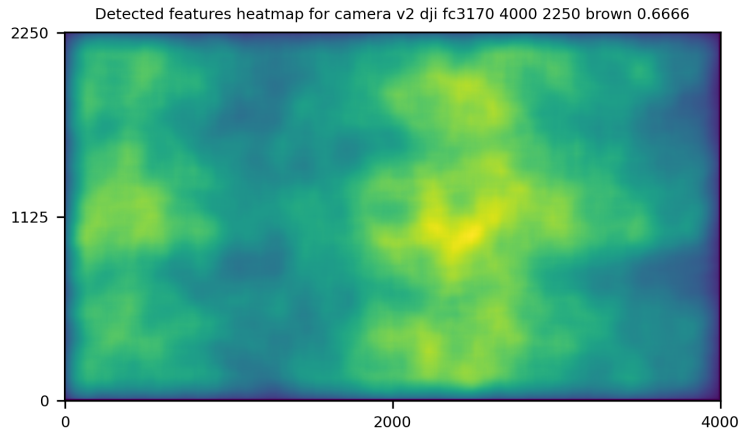
	Min.	Max.	Mean	Median
Detected	10041	18119	13079	13144
Reconstructed	1557	12501	5222	5148

Reconstruction Details

Average Reprojection Error (normalized / pixels / angular)	0.06 / 0.41 / 0.00014
Average Track Length	3.24 images
Average Track Length (> 2)	4.45 images
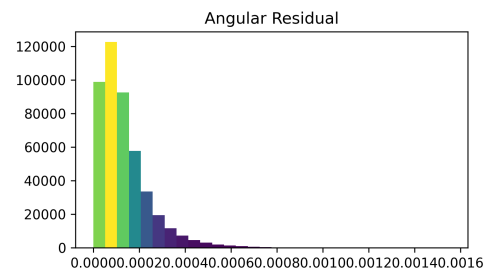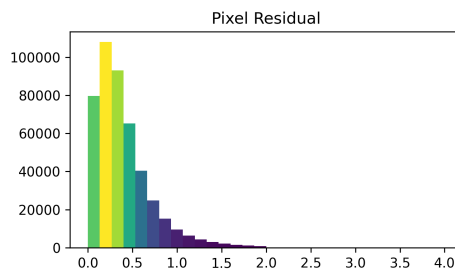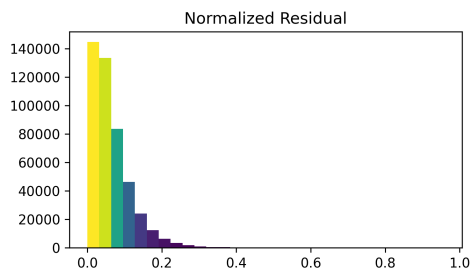
Tracks Details
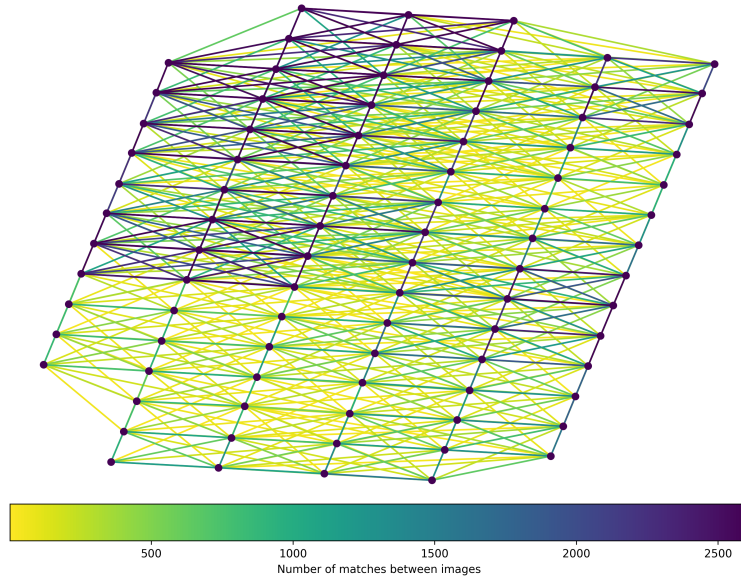
Length	2	3	4	5	6	7	8	9	10
Count	70032	27510	16715	11065	8348	3661	2453	1290	381

Camera Models Details

v2 dji fc3170 4000 2250 brown 0.6666

	k1	k2	k3	p1	p2	focal	aspect_ratio	cx	cy
Initial	0.0000	0.0000	0.0000	0.0000	0.0000	0.6667	1.0000	0.0000	0.0000
Optimized	-0.0282	0.0992	-0.0777	-0.0004	0.0002	0.6367	1.0000	-0.0003	-0.0067
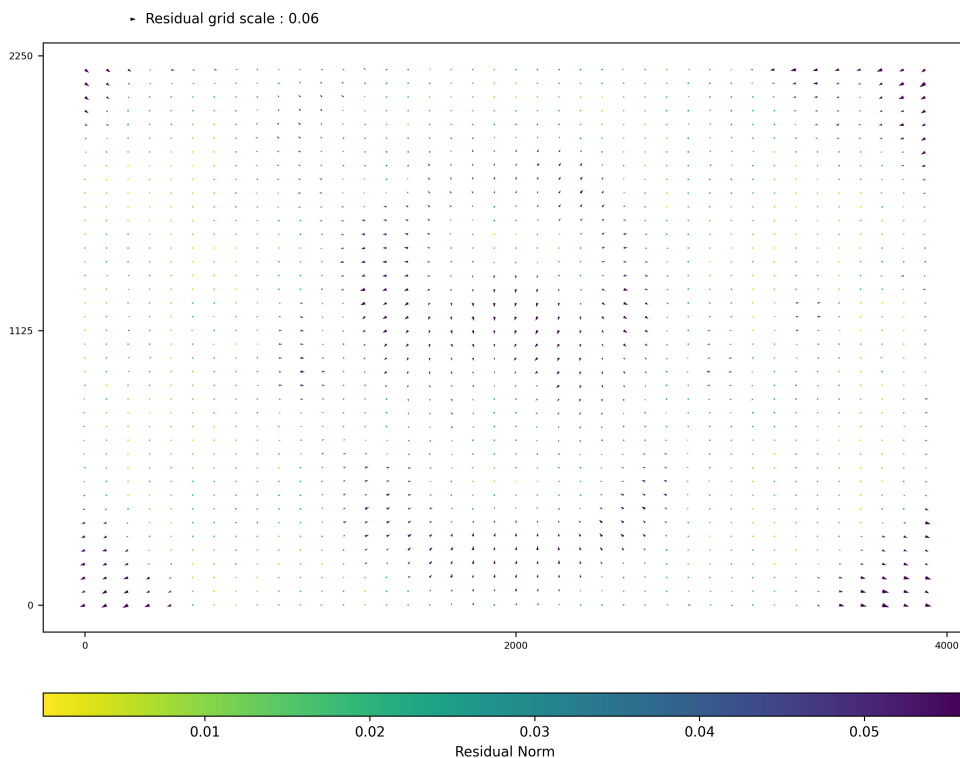
Aguçadoura Levantamento 4 GCPs

Processing Report
23 August 2022

Survey Data
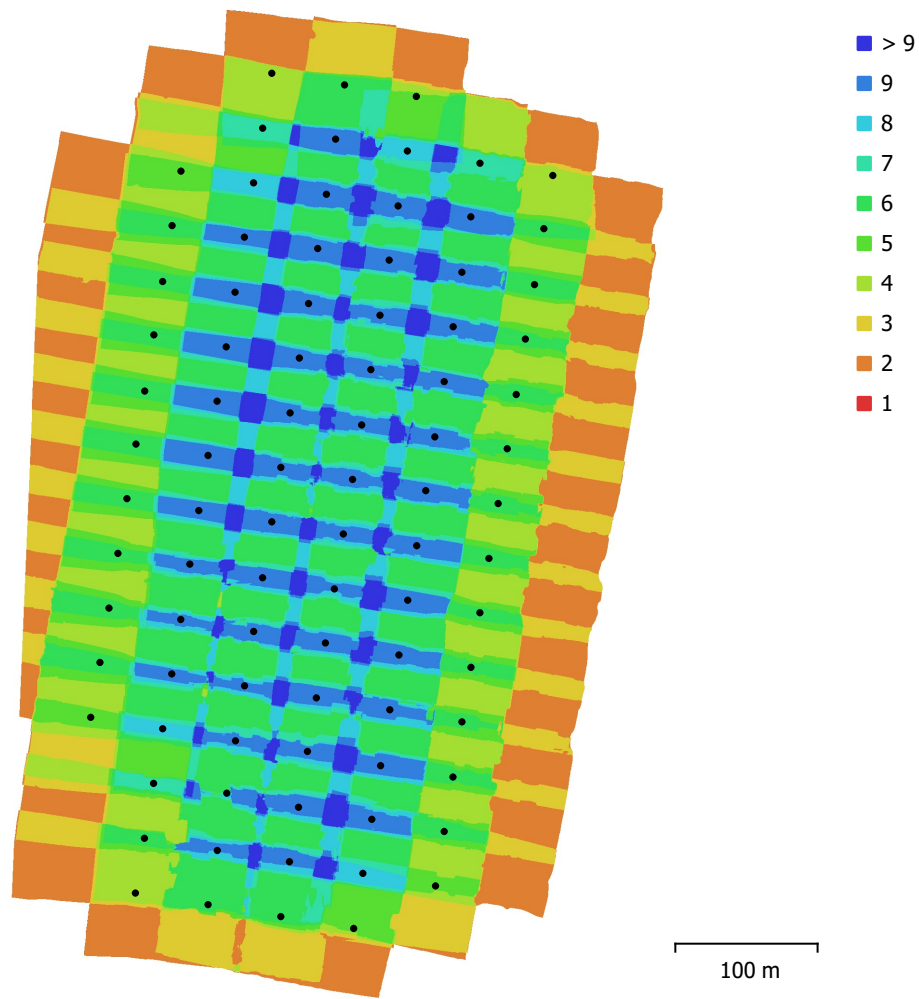
Fig. 1. Camera locations and image overlap.

Number of images:	88	Camera stations:	88
Flying altitude:	134 m	Tie points:	690,579
Ground resolution:	4.16 cm/pix	Projections:	1,864,094
Coverage area:	0.25 km²	Reprojection error:	0.389 pix

Camera Model	Resolution	Focal Length	Pixel Size	Precalibrated
FC3170 (4.5mm)	4000 x 2250	4.5 mm	1.77 x 1.77 µm	No

Table 1. Cameras.

Camera Calibration
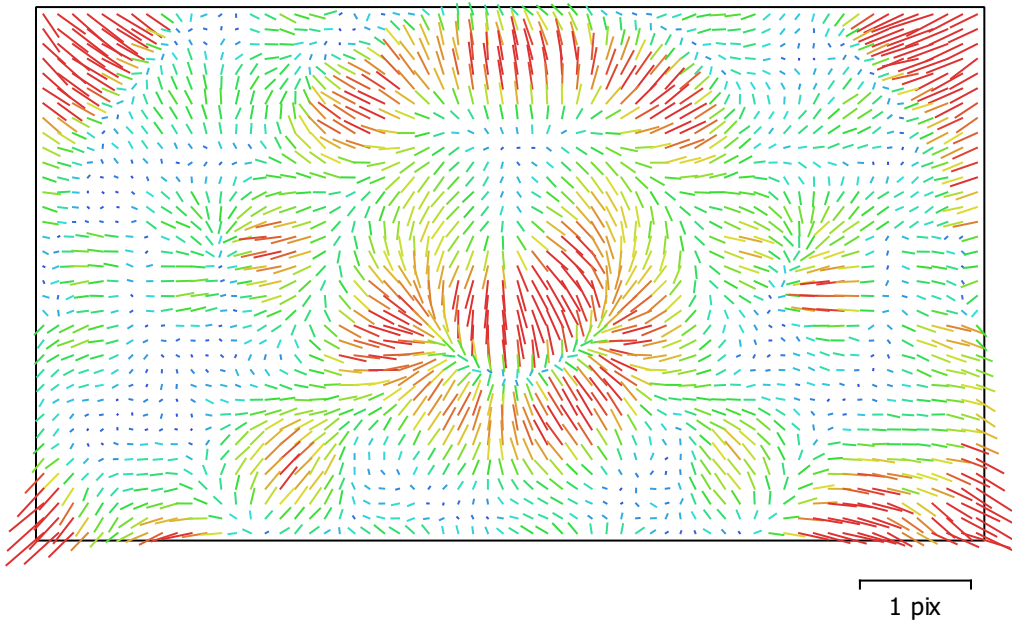
Fig. 2. Image residuals for FC3170 (4.5mm).

FC3170 (4.5mm)

88 images

Type	Resolution	Focal Length	Pixel Size
Frame	**4000 x 2250**	**4.5 mm**	**1.77 x 1.77 µm**

	Value	Error	F	Cx	Cy	B1	B2	K1	K2	K3	K4	P1	P2
F	**3009.94**	1.8	1.00	-0.47	0.34	-0.03	-0.04	-0.54	0.79	-0.70	0.36	0.03	-0.07
Cx	**-4.90032**	0.039		1.00	-0.17	0.01	0.02	0.24	-0.37	0.32	-0.16	0.36	0.01
Cy	**-25.8209**	0.023			1.00	-0.02	-0.05	-0.18	0.27	-0.23	0.11	-0.02	0.45
B1	**2.30818**	0.065				1.00	-0.01	-0.01	-0.00	-0.00	0.00	-0.04	0.09
B2	**3.28181**	0.066					1.00	0.02	-0.03	0.02	-0.01	-0.08	-0.04
K1	**-0.0434964**	7.8e-005						1.00	-0.90	0.91	-0.85	-0.05	0.04
K2	**0.24036**	0.00072							1.00	-0.98	0.83	0.03	-0.05
K3	**-0.325224**	0.0016								1.00	-0.91	-0.03	0.04
K4	**0.0913147**	0.0011									1.00	0.02	-0.02
P1	**0.000245404**	2.3e-006										1.00	-0.05
P2	**-0.0003311**	1.6e-006											1.00

Table 2. Calibration coefficients and correlation matrix.

Camera Locations
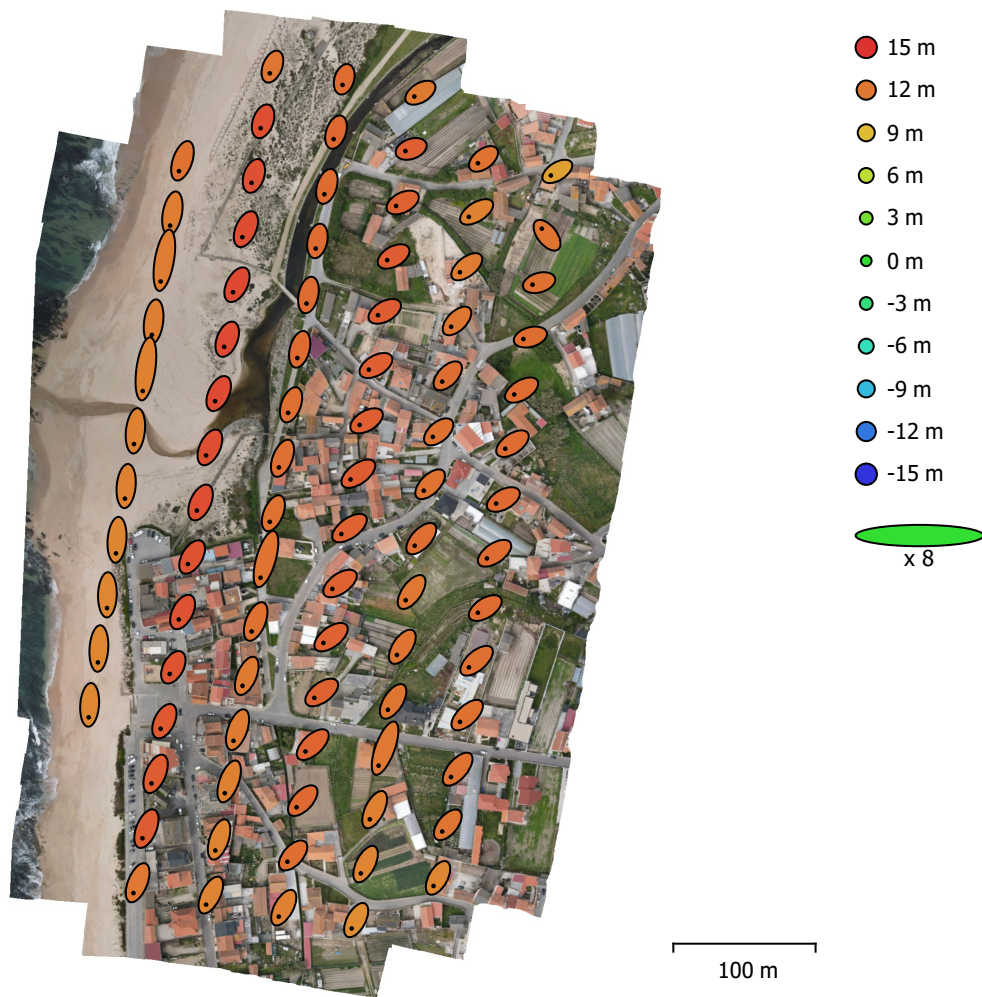
Fig. 3. Camera locations and error estimates.
Z error is represented by ellipse color. X,Y errors are represented by ellipse shape.
Estimated camera locations are marked with a black dot.

X error (m)	Y error (m)	Z error (m)	XY error (m)	Total error (m)
0.911483	1.56082	12.418	1.80747	12.5489

Table 3. Average camera location error.
X - Easting, Y - Northing, Z - Altitude.

Ground Control Points
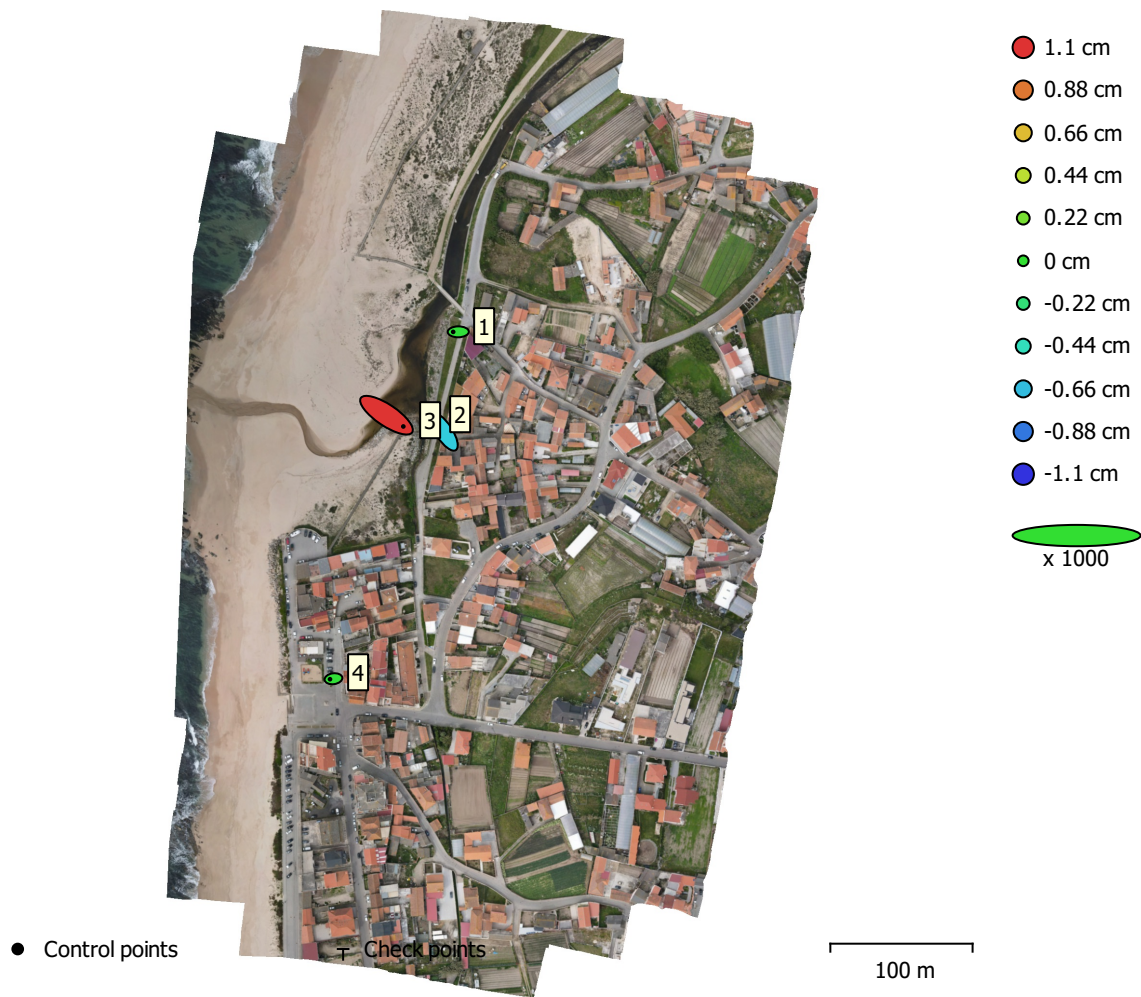
Fig. 4. GCP locations and error estimates.
Z error is represented by ellipse color. X,Y errors are represented by ellipse shape.
Estimated GCP locations are marked with a dot or crossing.

Count	X error (cm)	Y error (cm)	Z error (cm)	XY error (cm)	Total (cm)
4	1.35869	1.11923	0.62448	1.76032	1.86781

Table 4. Control points RMSE.
X - Easting, Y - Northing, Z - Altitude.

Label	X error (cm)	Y error (cm)	Z error (cm)	Total (cm)	Image (pix)
1	-0.717514	-0.00962359	-0.0262079	0.718057	0.221 (6)
2	-1.01282	1.57903	-0.601878	1.97013	0.155 (6)
3	2.36707	-1.58523	1.09389	3.05165	0.478 (4)
4	-0.490393	-0.065918	-0.0191261	0.495173	0.648 (9)
Total	**1.35869**	**1.11923**	**0.62448**	**1.86781**	**0.453**

Table 5. Control points.

X - Easting, Y - Northing, Z - Altitude.

Digital Elevation Model
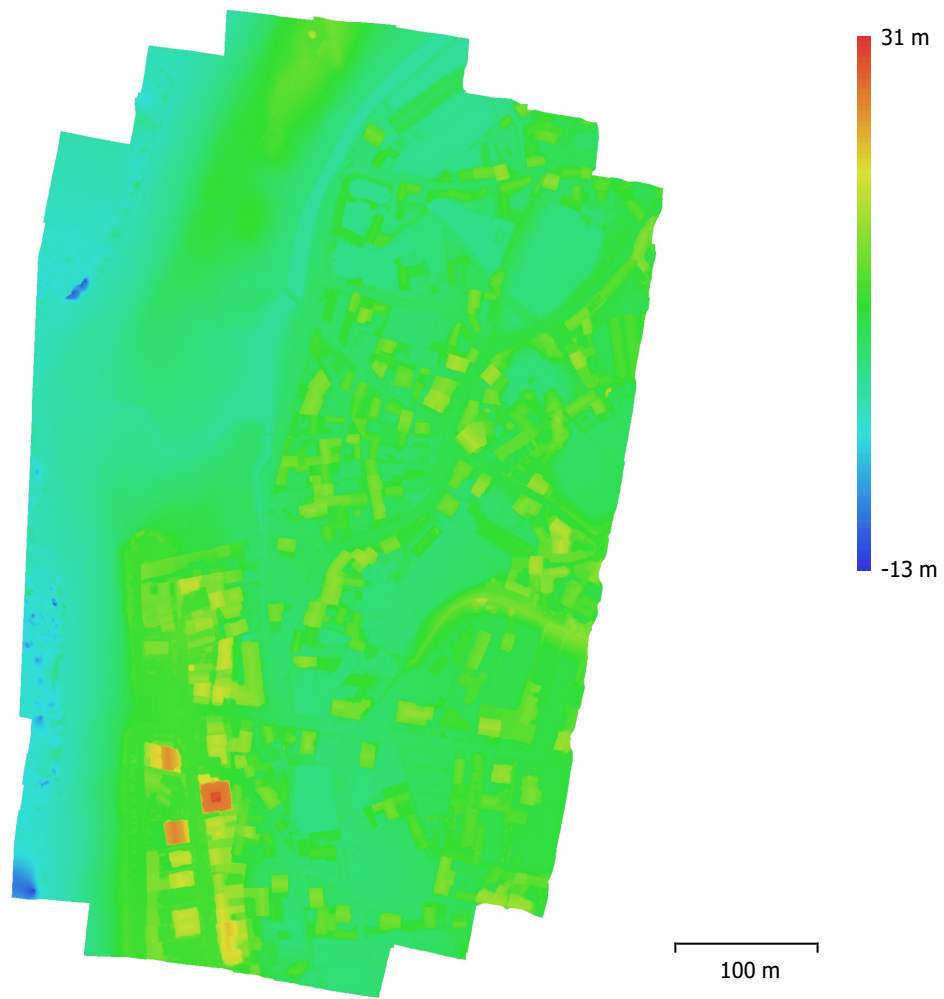
Fig. 5. Reconstructed digital elevation model.

Resolution: 8.32 cm/pix

Point density: 144 points/m²

Processing Parameters

General

Cameras	88
Aligned cameras	88
Markers	4
Coordinate system	ETRS89 / Portugal TM06 (EPSG::3763)
Rotation angles	Yaw, Pitch, Roll

Point Cloud

Points	690,579 of 708,605
RMS reprojection error	0.218034 (0.389036 pix)
Max reprojection error	1.0156 (22.736 pix)
Mean key point size	2.11585 pix
Point colors	3 bands, uint8
Key points	No
Average tie point multiplicity	2.73122

Alignment parameters

Accuracy	Highest
Generic preselection	Yes
Reference preselection	Yes
Key point limit	240,000
Tie point limit	0
Adaptive camera model fitting	No
Matching time	13 minutes 41 seconds
Alignment time	4 minutes 7 seconds

Optimization parameters

Parameters	f, cx, cy, k1-k3, p1, p2
Adaptive camera model fitting	Yes
Optimization time	29 seconds
Software version	1.5.3.8469

Depth Maps

Count	88

Depth maps generation parameters

Quality	High
Filtering mode	Mild
Processing time	2 minutes 25 seconds
Software version	1.5.3.8469

Dense Point Cloud

Points	43,689,673
Point colors	3 bands, uint8

Depth maps generation parameters

Quality	High
Filtering mode	Mild
Processing time	2 minutes 25 seconds

Dense cloud generation parameters

Processing time	3 minutes 39 seconds
Software version	1.5.3.8469

Model

Faces	8,682,318
Vertices	4,344,689
Vertex colors	3 bands, uint8
Texture	4,096 x 4,096, 4 bands, uint8

General
  Depth maps generation parameters
    Quality   High
    Filtering mode   Mild
    Processing time   2 minutes 25 seconds

General	
Depth maps generation parameters	
Quality	High
Filtering mode	Mild
Processing time	2 minutes 25 seconds
Reconstruction parameters	
Surface type	Height field
Source data	Dense cloud
Interpolation	Enabled
Strict volumetric masks	No
Processing time	2 minutes 38 seconds
Texturing parameters	
Mapping mode	Adaptive orthophoto
Blending mode	Mosaic
Texture size	4,096
Enable hole filling	Yes
Enable ghosting filter	Yes
UV mapping time	1 minutes 18 seconds
Blending time	3 minutes 44 seconds
Software version	1.5.3.8469
DEM	
Size	5,665 x 10,285
Coordinate system	ETRS89 / Portugal TM06 (EPSG::3763)
Reconstruction parameters	
Source data	Dense cloud
Interpolation	Enabled
Processing time	1 minutes 1 seconds
Software version	1.5.3.8469
Orthomosaic	
Size	11,010 x 16,678
Coordinate system	ETRS89 / Portugal TM06 (EPSG::3763)
Colors	3 bands, uint8
Reconstruction parameters	
Blending mode	Mosaic
Surface	DEM
Enable hole filling	Yes
Processing time	3 minutes 4 seconds
Software version	1.5.3.8469
Software	
Version	1.5.3 build 8469
Platform	Windows 64

General

  Depth maps generation parameters

Quality	High
Filtering mode	Mild
Processing time	2 minutes 25 seconds

  Reconstruction parameters

Surface type	Height field
Source data	Dense cloud
Interpolation	Enabled
Strict volumetric masks	No
Processing time	2 minutes 38 seconds

  Texturing parameters

Mapping mode	Adaptive orthophoto
Blending mode	Mosaic
Texture size	4,096
Enable hole filling	Yes
Enable ghosting filter	Yes
UV mapping time	1 minutes 18 seconds
Blending time	3 minutes 44 seconds

Software version   1.5.3.8469

DEM

Size	5,665 x 10,285
Coordinate system	ETRS89 / Portugal TM06 (EPSG::3763)

  Reconstruction parameters

Source data	Dense cloud
Interpolation	Enabled
Processing time	1 minutes 1 seconds

Software version   1.5.3.8469

Orthomosaic

Size	11,010 x 16,678
Coordinate system	ETRS89 / Portugal TM06 (EPSG::3763)
Colors	3 bands, uint8

  Reconstruction parameters

Blending mode	Mosaic
Surface	DEM
Enable hole filling	Yes
Processing time	3 minutes 4 seconds

Software version   1.5.3.8469

Software

Version	1.5.3 build 8469
Platform	Windows 64

Quality Report

Important: Click on the different icons for:

Help to analyze the results in the Quality Report

Additional information about the sections

Click here for additional tips to analyze the Quality Report

Summary

Project	202202V020
Processed	2022-02-19 23:07:22
Camera Model Name(s)	ZenmuseP1_35.0_8192x5460 (RGB)
Average Ground Sampling Distance (GSD)	1.51 cm / 0.59 in
Area Covered	0.840 km^2 / 83.9653 ha / 0.32 sq. mi. / 207.5903 acres

Quality Check

Images	median of 25254 keypoints per image	✓
Dataset	1464 out of 1493 images calibrated (98%), all images enabled	✓
Camera Optimization	0.19% relative difference between initial and optimized internal camera parameters	✓
Matching	median of 8030.18 matches per calibrated image	✓
Georeferencing	yes, 9 GCPs (9 3D), mean RMS error = 0.027 m	✓

Preview
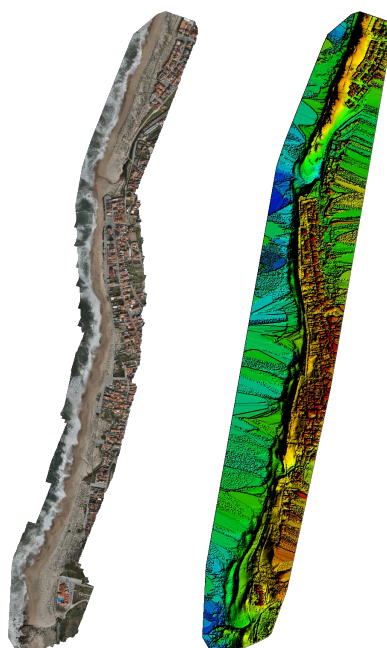
Figure 1: Orthomosaic and the corresponding sparse Digital Surface Model (DSM) before densification.

Calibration Details

Number of Calibrated Images	1464 out of 1493
Number of Geolocated Images	1493 out of 1493

? Initial Image Positions
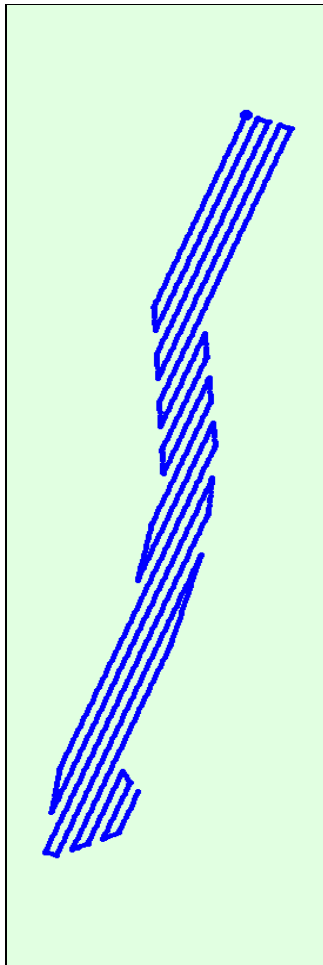
Figure 2: Top view of the initial image position. The green line follows the position of the images in time starting from the large blue dot.

? Computed Image/GCPs/Manual Tie Points Positions
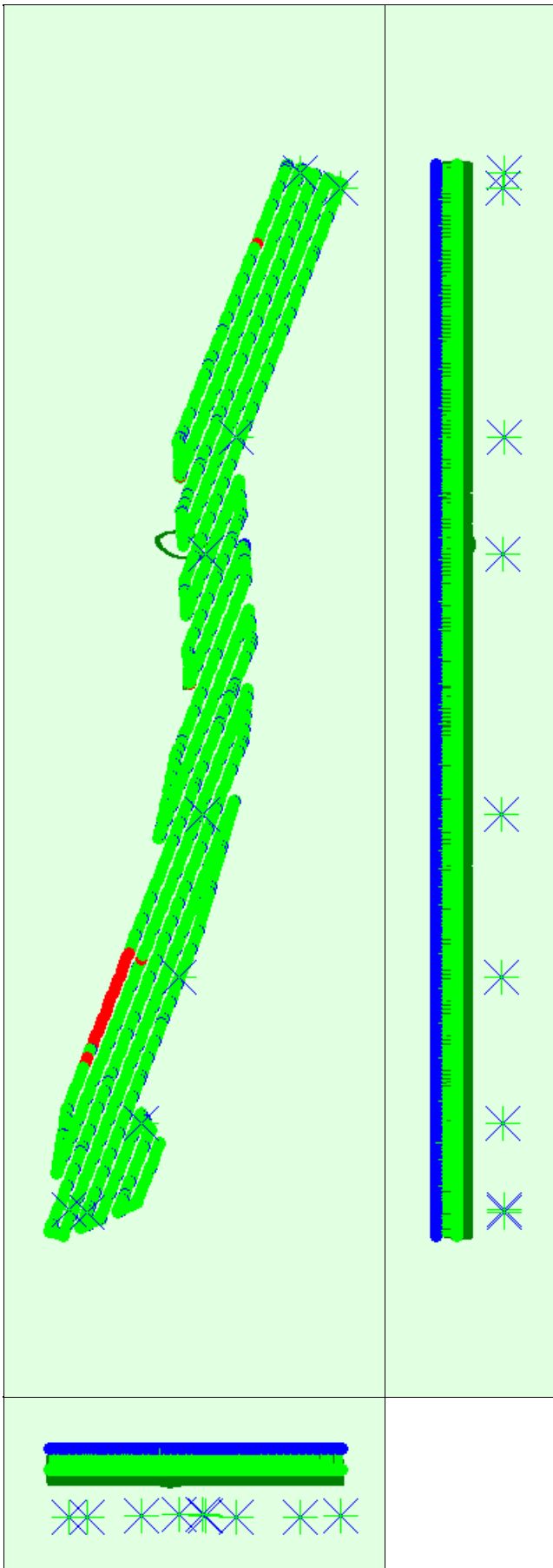
Uncertainty ellipses 1000x magnified

Figure 3: Offset between initial (blue dots) and computed (green dots) image positions as well as the offset between the GCPs initial positions (blue crosses) and their computed positions (green crosses) in the top-view (XY plane), front-view (XZ plane), and side-view (YZ plane). Red dots indicate disabled or uncalibrated images. Dark green ellipses indicate the absolute position uncertainty of the bundle block adjustment result.

Absolute camera position and orientation uncertainties

	X [m]	Y [m]	Z [m]	Omega [degree]	Phi [degree]	Kappa [degree]
Mean	0.005	0.005	0.038	0.003	0.003	0.003
Sigma	0.002	0.001	0.000	0.001	0.001	0.002

Overlap

Number of overlapping images: 1 2 3 4 5+
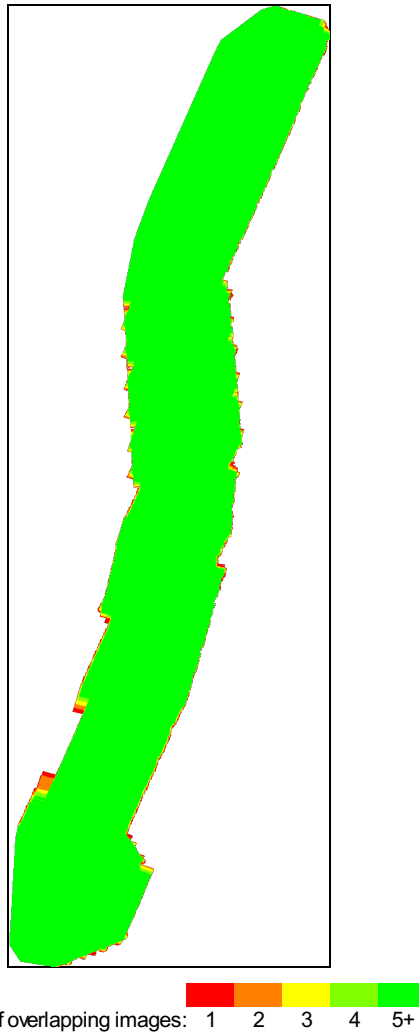
Figure 4: Number of overlapping images computed for each pixel of the orthomosaic.
Red and yellow areas indicate low overlap for which poor results may be generated. Green areas indicate an overlap of over 5 images for every pixel. Good quality results will be generated as long as the number of keypoint matches is also sufficient for these areas (see Figure 5 for keypoint matches).

Bundle Block Adjustment Details

Number of 2D Keypoint Observations for Bundle Block Adjustment	13250477
Number of 3D Points for Bundle Block Adjustment	3197039
Mean Reprojection Error [pixels]	0.077

Internal Camera Parameters

ZenmuseP1_35.0_8192x5460 (RGB). Sensor Dimensions: 35.000 [mm] x 23.328 [mm]

EXIF ID: ZenmuseP1_35.0_8192x5460

	Focal Length	Principal Point x	Principal Point y	R1	R2	R3	T1	T2
Initial Values	8194.340 [pixel] 35.010 [mm]	4096.001 [pixel] 17.500 [mm]	2729.996 [pixel] 11.664 [mm]	-0.048	0.021	-0.097	0.002	-0.001
Optimized Values	8178.710 [pixel] 34.943 [mm]	4061.288 [pixel] 17.352 [mm]	2753.976 [pixel] 11.766 [mm]	-0.048	0.033	-0.112	0.001	-0.002

Uncertainties (Sigma)	2.537 [pixel] 0.011 [mm]	0.126 [pixel] 0.001 [mm]	0.116 [pixel] 0.000 [mm]	0.000	0.001	0.001	0.000	0.000

The correlation between camera internal parameters determined by the bundle adjustment. White indicates a full correlation between the parameters, ie. any change in one can be fully compensated by the other. Black indicates that the parameter is completely independent, and is not affected by other parameters.

The number of Automatic Tie Points (ATPs) per pixel, averaged over all images of the camera model, is color coded between black and white. White indicates that, on average, more than 16 ATPs have been extracted at the pixel location. Black indicates that, on average, 0 ATPs have been extracted at the pixel location. Click on the image to the see the average direction and magnitude of the re-projection error for each pixel. Note that the vectors are scaled for better visualization. The scale bar indicates the magnitude of 1 pixel error.

2D Keypoints Table

	Number of 2D Keypoints per Image	Number of Matched 2D Keypoints per Image
Median	25254	8030
Min	11963	25
Max	47637	30432
Mean	25217	9051

3D Points from 2D Keypoint Matches

	Number of 3D Points Observed
In 2 Images	1404766
In 3 Images	605653
In 4 Images	338893
In 5 Images	217543
In 6 Images	158570
In 7 Images	108403
In 8 Images	68948
In 9 Images	53992
In 10 Images	44070
In 11 Images	36390
In 12 Images	30139
In 13 Images	25029
In 14 Images	16485
In 15 Images	13439
In 16 Images	11843
In 17 Images	11604
In 18 Images	12156
In 19 Images	11541
In 20 Images	7600
In 21 Images	4134

In 22 Images	2644
In 23 Images	2392
In 24 Images	2332
In 25 Images	2131
In 26 Images	1720
In 27 Images	961
In 28 Images	660
In 29 Images	558
In 30 Images	428
In 31 Images	389
In 32 Images	341
In 33 Images	330
In 34 Images	271
In 35 Images	209
In 36 Images	187
In 37 Images	99
In 38 Images	68
In 39 Images	44
In 40 Images	27
In 41 Images	18
In 42 Images	13
In 43 Images	8
In 44 Images	6
In 45 Images	4
In 46 Images	1

2D Keypoint Matches
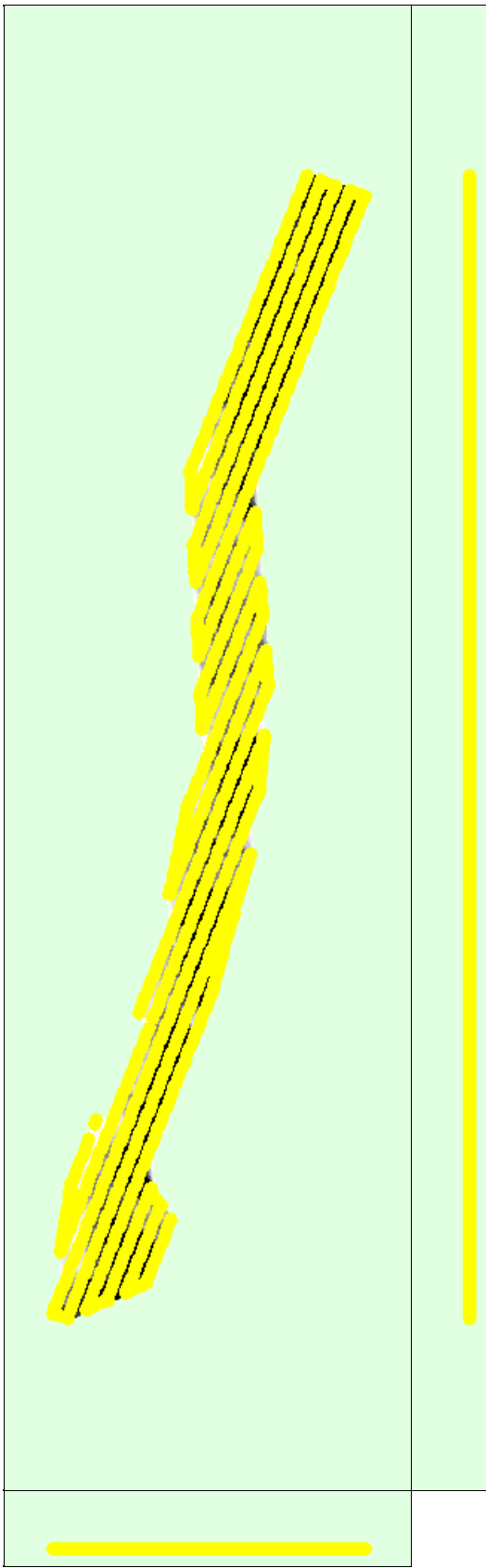
Number of matches

25 222 444 666 888 1111 1333 1555 1777 2000

Figure 5: Computed image positions with links between matched images. The darkness of the links indicates the number of matched 2D keypoints between the images. Bright links indicate weak links and require manual tie points or more images.

Geolocation Details

❓ Ground Control Points ⓘ

GCP Name	Accuracy XY/Z [m]	Error X [m]	Error Y [m]	Error Z [m]	Projection Error [pixel]	Verified/Marked
10 (3D)	0.020/ 0.020	-0.008	-0.011	-0.007	0.204	12 / 12
12 (3D)	0.020/ 0.020	-0.002	-0.011	-0.026	0.241	15 / 15
13 (3D)	0.020/ 0.020	0.011	0.019	-0.041	0.217	10 / 10
15 (3D)	0.020/ 0.020	0.003	0.014	-0.013	0.263	13 / 13
20 (3D)	0.020/ 0.020	0.020	0.005	-0.005	0.266	16 / 16
27 (3D)	0.020/ 0.020	-0.045	-0.006	0.033	0.180	13 / 13
30 (3D)	0.020/ 0.020	0.047	-0.003	0.026	0.369	19 / 19
31 (3D)	0.020/ 0.020	0.027	-0.060	0.014	0.182	11 / 11
33 (3D)	0.020/ 0.020	-0.054	0.053	0.028	0.413	15 / 15
Mean [m]		-0.000132	-0.000030	0.000987		
Sigma [m]		0.030804	0.028536	0.024488		
RMS Error [m]		0.030804	0.028536	0.024508		

Localisation accuracy per GCP and mean errors in the three coordinate directions. The last column counts the number of calibrated images where the GCP has been automatically verified vs. manually marked.

❓ Absolute Geolocation Variance ⓘ

Min Error [m]	Max Error [m]	Geolocation Error X [%]	Geolocation Error Y [%]	Geolocation Error Z [%]
-	-0.04	0.07	0.07	0.14
-0.04	-0.03	0.00	0.07	0.55
-0.03	-0.02	0.07	0.00	0.62
-0.02	-0.02	0.00	0.14	2.40
-0.02	-0.01	0.21	0.14	9.99
-0.01	0.00	48.32	49.62	33.88
0.00	0.01	50.99	49.69	39.90
0.01	0.02	0.21	0.00	9.72
0.02	0.02	0.00	0.07	1.92
0.02	0.03	0.07	0.07	0.34
0.03	0.04	0.00	0.07	0.27
0.04	-	0.07	0.07	0.27
Mean [m]		0.681864	0.147030	53.891737
Sigma [m]		0.002555	0.002827	0.008937
RMS Error [m]		0.681869	0.147057	53.891738

Min Error and Max Error represent geolocation error intervals between -1.5 and 1.5 times the maximum accuracy of all the images. Columns X, Y, Z show the percentage of images with geolocation errors within the predefined error intervals. The geolocation error is the difference between the initial and computed image positions. Note that the image geolocation errors do not correspond to the accuracy of the observed 3D points.

Geolocation Bias	X	Y	Z
Translation [m]	0.681862	0.147018	53.891779

Bias between image initial and computed geolocation given in output coordinate system.

❓ Relative Geolocation Variance ⓘ

Relative Geolocation Error	Images X [%]	Images Y [%]	Images Z [%]
[-1.00, 1.00]	99.66	99.38	97.26
[-2.00, 2.00]	99.73	99.66	99.66
[-3.00, 3.00]	99.86	99.73	100.00
Mean of Geolocation Accuracy [m]	0.011904	0.011904	0.021819
Sigma of Geolocation Accuracy [m]	0.000567	0.000567	0.000976

Images X, Y, Z represent the percentage of images with a relative geolocation error in X, Y, Z.

Geolocation Orientational Variance	RMS [degree]
Omega	118.928
Phi	0.975
Kappa	31.639

Geolocation RMS error of the orientation angles given by the difference between the initial and computed image orientation angles.

Initial Processing Details ⓘ

System Information ⓘ

Hardware	CPU: Intel(R) Xeon(R) W-2255 CPU @ 3.70GHz RAM: 32GB GPU: unknown graphics card (Driver: unknown)
Operating System	Windows 10 Pro for Workstations, 64-bit

Coordinate Systems ⓘ

Image Coordinate System	WGS 84
Ground Control Point (GCP) Coordinate System	ETRS89 / Portugal TM06
Output Coordinate System	ETRS89 / Portugal TM06

Processing Options ⓘ

Detected Template	No Template Available
Keypoints Image Scale	Full, Image Scale: 0.5
Advanced: Matching Image Pairs	Aerial Grid or Corridor
Advanced: Matching Strategy	Use Geometrically Verified Matching: no
Advanced: Keypoint Extraction	Targeted Number of Keypoints: Automatic
Advanced: Calibration	Calibration Method: Standard Internal Parameters Optimization: All External Parameters Optimization: All Rematch: Auto, no

Point Cloud Densification details ⓘ

Processing Options ⓘ

Image Scale	multiscale, 1/2 (Half image size, Default)
Point Density	Optimal
Minimum Number of Matches	3
3D Textured Mesh Generation	no
LOD	Generated: no
Advanced: Image Groups	group1
Advanced: Use Processing Area	yes
Advanced: Use Annotations	yes
Time for Point Cloud Densification	03h:24m:41s
Time for Point Cloud Classification	NA
Time for 3D Textured Mesh Generation	NA

Results ⓘ

Number of Processed Clusters	9
Number of Generated Tiles	11

Number of 3D Densified Points	257292197
Average Density (per m^3)	455.1

DSM, Orthomosaic and Index Details ⓘ

Processing Options ⓘ

DSM and Orthomosaic Resolution	1 x GSD (1.51 [cm/pixel])
DSM Filters	Noise Filtering: yes Surface Smoothing: yes, Type: Sharp
Raster DSM	Generated: yes Method: Inverse Distance Weighting Merge Tiles: yes
Orthomosaic	Generated: yes Merge Tiles: yes GeoTIFF Without Transparency: no Google Maps Tiles and KML: no
Time for DSM Generation	02h:04m:33s
Time for Orthomosaic Generation	07h:37m:37s
Time for DTM Generation	00s
Time for Contour Lines Generation	00s
Time for Reflectance Map Generation	00s
Time for Index Map Generation	00s